THERMO-VISCOELASTIC ANALYSIS OF COMPOSITE MATERIALS

FINAL REPORT

Prepared for

NASA Langley Research Center

Under

NASA Grant No. NAG-1-621

By

K. Y. Lin and I. H. Hwang

Department of Aeronautics and Astronautics
University of Washington, FS-10
Seattle, Washington 98195

June 1988

THERMO-VISCOELASTIC ANALYSIS
OF COMPOSITE MATERIALS

FINAL REPORT

Prepared for

NASA Langley Research Center

Under

NASA Grant No. NAG-1-621

By

K. Y. Lin and I. H. Hwang

Department of Aeronautics and Astronautics
University of Washington, FS-10
Seattle, Washington 98195

June 1988

FOREWORD

TABLE OF CONTENTS

1. INTRODUCTION

Advanced composite materials, especially graphite/epoxy, are being applied to airplane structures in order to improve performance and save weight. An important consideration in composite design is the residual strength of a structure containing holes, delaminations or interlaminar damage when subjected to compressive loads. While elastic behavior of composites has been studied extensively in recent years, the viscoelastic response of these materials is not well understood. Recent studies by several investigators have revealed the importance of viscoelastic effects in polymer-based composites [1-4]. The viscoelastic effect is particularly significant at elevated temperature/moisture conditions since the matrix material is strongly affected by the environment.

The solution of viscoelastic problems in composites has been limited to special cases which can be solved by classical lamination theory [2-4]. In this report, a finite element procedure is presented for calculating time-dependent stresses and strains in composite structures with general configurations and complicated boundary conditions. Using this procedure the in-plane and interlaminar stress distributions and histories in notched and unnotched composites have been obtained for mechanical and thermal loads. Both two-dimensional and three-dimensional viscoelastic problems are analyzed. The effects of layup orientation and load spectrum on creep response and stress relaxation have also been studied.

2. CONSTITUTIVE EQUATIONS FOR ANISOTROPIC VISCOELASTIC MATERIALS

Consider a linear anisotropic viscoelastic material subjected to both mechanical and thermal loads. Using the contracted notation for the stresses and strains, the constitutive relations may be written in the following integral form [5]:

$$\sigma_i(t) = \int_{-\infty}^{t} C_{ij}(T, t-\tau) \frac{\partial \overline{\varepsilon}_j(\tau)}{\partial \tau} \, d\tau \tag{1}$$

$$\text{with } \overline{\varepsilon}_j = \varepsilon_j - \varepsilon_j^*$$

In the above, σ_i and ε_j are the stress and the total strain components along the principal material directions (123 axes). C_{ij} are the relaxation moduli, T is temperature and t is time. ε_j^* is the thermal strain component in the stress-free state and can be expressed as a function of the coefficient of thermal expansion α_j and the stress-free temperature T^* by

$$\varepsilon_j^* = \int_{T^*}^{T} \alpha_j(T) \, dT \tag{2}$$

In this study the α_j is assumed to be independent of time and temperature, that is, $\varepsilon_j^* = \alpha_j \Delta T$ with $\Delta T = T - T^*$.

The basic viscoelastic properties C_{ij} can be determined from the experimental characterization of a unidirectional composite at various temperatures over a long period of time. However, this technique is quite time consuming and an alternate technique based on the time/temperature superposition is frequently used to minimize the test time required for polymer based composites. The alternate technique consists of testing a series of specimens at higher temperatures. The test results are plotted and

2

the resulting curves are then shifted horizontally (and sometimes also vertically) with respect to a reference temperature to obtain the master relaxation curves for the C_{ij} components. The amount the curves are shifted is termed the shift factor ϕ_{ij}. Materials whose viscoelastic properties can be characterized using this procedure are referred to as thermorheologically simple materials. For this special class of materials the relaxation functions C_{ij} in the principal material directions may be represented in the following form

$$C_{ij}(T,t) = C_{ij}(T_0, \zeta_{ij}) \tag{3}$$

where T_0 is the reference temperature for the master curves and ζ_{ij} is the reduced time. The reduced time is related to the shift factor $\phi_{ij}(T)$ by

$$\zeta_{ij}(t) = \int_0^t \phi_{ij}(T(s))\, ds \tag{4}$$

As in the elastic case the relaxation functions $\overline{C}_{ij}$ along the load directions xyz (Fig. 1) can be obtained from the C_{ij} of the principal material directions (123) by the use of tensor transformations. With the transformed $\overline{C}_{ij}$, the viscoelastic constitutive equation for an anisotropic material along the xyz coordinates becomes

$$\sigma_i(t) = \int_{-\infty}^t \overline{C}_{ij}(T_0,\ \zeta_{ij}(t) - \zeta_{ij}'(\tau)) \frac{\partial \varepsilon_j(\tau)}{\partial \tau}\, d\tau \tag{5}$$

where

$$\zeta_{ij}'(\tau) = \int_0^\tau \phi_{ij}(T(s))\, ds \tag{6}$$

3

3. VARIATIONAL THEOREM FOR LINEAR THERMO-VISCOELASTICITY

A variational theorem for linear viscoelastic materials is given by Christensen [6] and is extended here to include nonisothermal effects. For an anisotropic material the functional π can be defined as

$$\pi = \int_V \int_{s=-\infty}^{s=t} \int_{\tau=-\infty}^{\tau=t-s} \left\{ \frac{1}{2} \, \overline{C}_{ij}(T,t-s-\tau) \, \frac{\partial \varepsilon_i(\tau)}{\partial \tau} \, \frac{\partial \varepsilon_j(s)}{\partial s} - \overline{C}_{ij}(T,t-s-\tau) \, \frac{\partial \varepsilon_i^*(\tau)}{\partial \tau} \, \frac{\partial \varepsilon_j(s)}{\partial s} \right\} \, d\tau \, ds \, dV$$

(7)

$$- \int_{S_\sigma} \int_{s=-\infty}^{s=t} \overline{T}_i(t-s) \, \frac{\partial u_i(s)}{\partial s} \, ds \, dA$$

where V is the volume domain, u_i is the displacement, and S_σ is the portion of boundary where the traction $\overline{T}_i$ is prescribed.

Taking the first variation of π and letting $\delta\pi = 0$ along with the commutative relations of Stieltjes convolution yields

$$\delta\pi = \int_{s=-\infty}^{s=t} \left\{ \int_V \sigma_i(t-s) \, \frac{\partial \delta\varepsilon_i(s)}{\partial s} \, dV - \int_{S_\sigma} \overline{T}_i(t-s) \, \frac{\partial \delta u_i(s)}{\partial s} \, dA \right\} \, ds = 0 \qquad (8)$$

The solution to the quasi-static thermo-viscoelastic boundary value problem is found by extremizing the functional π [6,7]. This variational method will be used in the following finite element formulation.

4. FINITE ELEMENT FORMULATION

Consider a symmetric laminate with arbitrary ply orientations subjected to both mechanical and thermal loads. It is assumed that the prescribed temperature is uniform throughout the laminate at any time instant and that the applied surface traction is separable function of position and time. These assumptions allow the displacement solutions to be expressed as the product of two separate functions, one involving only spatial coordinates and the other involving only spatial coordinates and the other involving the time variable.

In the finite element development, 4-node quadrilateral 2-D elements and 8-node 3-D solid elements are considered. Using an isoparametric formulation the displacement fields within an element are interpolated as

$$\{ u \} = [N] \{ q \} \tag{9}$$

where $\{ q \}$ is a nodal displacement vector whose components are a function of time only. The strains $\{\varepsilon\}$ can be obtained by the differentiation of the displacement field in Eq. (9) and are expressed as

$$\{ \varepsilon \} = [B] \{ q \} \tag{10}$$

Use of Eqs. (9) and (10) and the variational theorem discussed in Eq. (8) leads to the following equilibrium equation for an element

$$\int_{-\infty}^{t} \int_{\Omega} B_{im} \, \mathcal{C}_{ij}(T, t-\tau) \, B_{jn} \, d\Omega \, \frac{\partial q_n(\tau)}{\partial \tau} \, d\tau$$

$$= \int_{-\infty}^{t} \int_{\Omega} B_{im} \, \mathcal{C}_{ij} (T, t-\tau) \, \frac{\partial \varepsilon_j^*(\tau)}{\partial \tau} d\tau \, d\Omega + \int_{\Gamma_\sigma} N_{km} \, \tilde{T}_k(t) \, d\Gamma \tag{11}$$

where Ω is the volume of the element.

Note that the first term on the right hand side of Eq. (11) is the force vector due to thermal loading and the second term is the reactive force vector. When Eq. (11) is assembled the reactive force vector vanishes everywhere except on the boundary where the traction is prescribed.

Before proceeding further, the following abbreviations for C_{ij} of a unidirectional ply are defined as

$$C_1 = C_{11}, \; C_2 = C_{12}, \; C_3 = C_{13}, \; C_4 = C_{22}, \; C_5 = C_{23},$$
$$C_6 = C_{33}, \; C_7 = C_{44}, \; C_8 = C_{55}, \; C_9 = C_{66} \tag{12}$$

These nine relaxation functions are expanded in terms of exponential series so that the integral equation (11) may be easily calculated [3,7]. The exponential series is

$$C_i(t) = C_{io} + \sum_{\omega=1}^{NT} C_{i\omega} \exp(-t/\lambda_{i\omega}) \tag{13}$$

where $\lambda_{i\omega}$ is the relaxation time obtained from the master curve. The $\bar{C}_{ij}$ with respect to the xyz axes can be obtained with the use of tensor transformation. The results are

$$\bar{C}_{ij}(t) = \sum_{r=1}^{9} n_{ijr} \, C_r(t) \tag{14}$$

where n_{ijr} is the component of the transformation coefficient matrix for each layer. Note that n_{ijr} is symmetric with respect to indices i and j. The full expressions for n_{ijr} are given in Appendix A.

From Eq. (11) the equation for the element stiffness matrix k_{mn} of an element is

$$k_{mn}(t-\tau) = \int_\Omega B_{im} \overline{C}_{ij}(T, t - \tau) B_{jn} \, d\Omega$$

$$= \sum_{r=1}^{9} \left\{ k_{mnr,o} + \sum_{\omega=1}^{NT} k_{mnr,\omega} \exp[-(\zeta_r - \zeta_r')/\lambda_{r\omega}] \right\} \tag{15}$$

where $k_{mnr,\omega}$ is

$$k_{mnr,\omega} = C_{r\omega} \int_\Omega B_{im} n_{ijr} B_{jn} \, d\Omega \tag{16}$$

Similar to the elastic case, the element stiffness matrix and force vector are assembled over the whole domain to yield the following global equation for the displacement $u_n(t)$:

$$K_{mn}(\zeta) u_n(0) + \int_0^t K_{mn}(\zeta - \zeta') \frac{\partial u_n(\tau)}{\partial \tau} \, d\tau = F_m^t(t) + F_m^r(t) \tag{17}$$

where

$$K_{mn}(\zeta - \zeta') = \sum_{r=1}^{9} \left\{ K_{mnr,o} + \sum_{\omega=1}^{NT} K_{mnr,\omega} \exp[-(\zeta_r - \zeta_r')/\lambda_{r\omega}] \right\} \tag{18}$$

and m, n = 1, 2, 3, ..., NDT, NDT = total number of degrees of freedom.

In the above, $K_{mnr,\omega}$ is associated with the global stiffness matrix, $F_m^t(t)$ is the component of the global residual force vector due to thermal load and $F_m^r(t)$ is the component of the global force vector due to the prescribed tractions.

A direct integration of Eq. (17) requires enormous computer storage space for the stiffness matrices and the displacement vectors of previous times and is not feasible in most problems of practical interest. To overcome the storage limitations and reduce computing time, a numerical scheme similar to that employed by Taylor et al. [7] for an isotropic material is used. Eq. (17) can then be replaced by a summation of the integrations over a series of time intervals Δt. Within each subinterval of time the dependent variables $u_n(t)$ may be approximated by a linear variation. That is,

7

$$\frac{\partial u_n(t)}{\partial t} \cong \frac{\Delta u_n(t_j)}{\Delta t}, \quad \text{for } t_{j-1} < t < t_j \tag{19}$$

where
$$\Delta u_n(t_j) = u_n(t_j) - u_n(t_{j-1}). \tag{20}$$

Using the above approximation for the derivatives of $u_n(t)$, Eq. (17) at $t = t_p$ becomes

$$\sum_{j=1}^{p} \int_{t_{j-1}}^{t_j} \sum_{r=1}^{9} \{K_{mnr,o} + \sum_{\omega=1}^{NT} K_{mnr,\omega} \exp[-(\zeta_{r,p} - \zeta_r')/\lambda_{r\omega}]\} \, d\tau \; \frac{\Delta u_n(t_j)}{\Delta t_j} \tag{21}$$

$$= F_m^t(t_p) + F_m^r(t_p) - \sum_{r=1}^{9} \{K_{mnr,o} + \sum_{\omega=1}^{NT} K_{mnr,\omega} \exp(-\zeta_{r,p}/\lambda_{r\omega})\} \, u_n(0)$$

where $\zeta_{r,p} = \zeta_r(t_p)$.

Finally Eq. (21) leads to a set of algebraic equations

$$\sum_{r=1}^{9} \{K_{mnr,o} + \sum_{\omega=1}^{NT} K_{mnr,\omega} \, h_{r\omega}(\Delta t_p)\} \, \Delta u_n(t_p) = F_m^t(t_p) + F_m^r(t_p) \tag{22}$$

$$- \sum_{r=1}^{9} K_{mnr,o} \, u_n(t_{p-1}) - \sum_{r=1}^{9} \sum_{\omega=1}^{NT} g_{mr,\omega}(t_p)$$

where

$$h_{r\omega}(\Delta t_j) = \frac{1}{\Delta t_j} \int_{t_{j-1}}^{t_j} \exp[-(\zeta_{r,j} - \zeta_r')/\lambda_{r\omega}] \, d\tau \tag{23}$$

$$g_{mr,\omega}(t_p) = K_{mnr,\omega} \exp(-\zeta_{r,p}/\lambda_{r\omega}) \, u_n(0) \tag{24}$$

$$+ \sum_{j=1}^{p-1} K_{mnr,\omega} \exp[-(\zeta_{r,p} - \zeta_{r,j})/\lambda_{r\omega}] \, h_{r\omega}(\Delta t_j) \Delta u_n(t_j)$$

If the temperature is constant within the time interval Δt_j, $h_{r\omega}(\Delta t_j)$ can be evaluated exactly as follows

$$h_{r\omega}(\Delta t_j) = \lambda_{r\omega}[1 - \exp(-\Delta\zeta_{r,j}/\lambda_{r\omega})] / \Delta\zeta_{r,j} \qquad (25)$$

where $\qquad \Delta\zeta_{r,j} = \zeta_{r,j} - \zeta_{r,j-1} \qquad (26)$

If the temperature is not constant during Δt_j, the shift factor corresponding to the specific temperature variation within the time interval can be used to obtain the reduced time from Eq. (4), from which $h_{r\omega}(\Delta t_j)$ can be determined numerically.

Using Eq. (24), a general recursive expression can be derived for $p > 1$. The recursive formula is

$$g_{mr,\omega}(t_p) = \exp(-\Delta\zeta_{r,p}/\lambda_{r\omega})[g_{mr,\omega}(t_{p-1}) + K_{mnr,\omega} \, h_{r\omega}(\Delta t_{p-1}) \, \Delta u_n(t_{p-1})] \qquad (27)$$

with

$$g_{mr,\omega}(t_0) = 0, \quad h_{r\omega}(\Delta t_0) = 1, \text{ and } \Delta u_n(t_0) = u_n(0).$$

The residual thermal force vector can be updated using a numerical algorithm similar to that used for the stiffness matrix. The element residual thermal force vector represented by the first term on the right-hand side of Eq. (11) is expressed as

$$f_m^t(t) = \int_{-\infty}^t \int_\Omega B_{im} \sum_{r=1}^9 n_{ijr} \left\{ C_{ro} + \sum_{\omega=1}^{NT} C_{r\omega} \exp[-(\zeta_r - \zeta_r')/\lambda_{r\omega}] \right\} \bar{\alpha}_j \, \frac{\partial \Delta T(\tau)}{\partial \tau} \, d\Omega \, d\tau$$

$$= \sum_{r=1}^9 \int_{-\infty}^t \left\{ f_{mro} + \sum_{\omega=1}^{NT} f_{mr\omega} \exp[-(\zeta_r - \zeta_r')/\lambda_{r\omega}] \right\} \frac{\partial \Delta T(\tau)}{\partial \tau} \, d\tau \qquad (28)$$

where

$$f_{mr\omega} = \int_\Omega B_{im} \left(n_{ijr} \, C_{r\omega} \, \bar{\alpha}_j \right) d\Omega \qquad (29)$$

The $\bar{\alpha}_j$ are the coefficients of thermal expansion along the xyz axes. These force vectors can be assembled to obtain the global residual thermal force vector $F_m^t(t)$ in Eq. (21).

9

For the non-isothermal case, the solution procedure is to descretize temperature histories so that the temperature change occurs only in elastic time step A-A' ($\Delta t = 0$) with the temperature remaining constant during the subsequent viscoelastic time step A'-B (See Fig. 2). Within the time step A-A', the reduced time is not changed and $h_{r\omega}(\Delta t_j) = 1$. During the viscoelastic time step A'-B, the difference in the reduced time $\Delta \zeta_r(t_j)$ is determined from the time difference Δt_j multiplied by the corresponding shift factor. Eq. (25) is then used to calculate $h_{r\omega}(\Delta t_j)$.

After Eq. (22) is solved for Δu_n, the nodal displacements at current time t_p are obtained from the relation $u_n(t_p) = u_n(t_{p-1}) + \Delta u_n(t_p)$. Once the displacements are found, the strain field can be determined. Finally, the viscoelastic constitutive relations in Eq. (5) are used to calculate the stresses.

It is noted that the above formulation is valid for general 3-D viscoelastic problems. In the special case of a 2-D analysis, the $\overline{C}_{ij}$ matrix of each layer is reduced to $\overline{Q}_{ij}$ and is averaged through the laminate thickness to obtain the extensional stiffness matrix A_{ij}. Also note that the approximation of the dependent variables $u_n(t)$ by a linear Lagrangian interpolation function may cause significant error accumulations since the solution at the current time is affected by the previous solutions. Such error is expected to grow as the number of solution iterations increases. In order to minimize the error accumulation, higher order interpolation functions are needed. However, such a formulation becomes extremely complex and cumbersome since more than one set of previous solutions are required to obtain the current solutions.

5. NUMERICAL RESULTS FOR THE TIME-DEPENDENT RESPONSE

Numerical results on time-dependent stress/strain fields are obtained for graphite/epoxy composites using the formulation derived in the previous sections. Elastic material properties used in the analysis are those typical of graphite/epoxy composites as shown in Table 1. With these engineering material constants, the elastic stiffness matrix $[C_{ij}(0)]$ can be obtained. Viscoelastic relaxation functions $C_{ij}(t)$ are then generated by multiplying the elastic stiffness $C_{ij}(0)$ by specific time varying functions. In this study, the C_{11} is assumed to be independent of time and temperature while other relaxation functions are assumed to have the same time-varying function $f(t)$. The function $f(t)$ is taken from Flaggs and Crossman's experimental curve [3,8] and is expressed in terms of an exponential series containing 11 terms (See Table 2). The shift factors corresponding to various temperatures as given in [8] are the same for all $C_{ij}(t)$ master curves. The stress free temperature for the graphite/epoxy laminate is assumed to be 350°F. The shift factors at various temperatures are shown in Table 3.

5.1 Unnotched Laminates

The first analysis is to verify the accuracy of the present approach by comparing solutions with the incremental classical lamination theory (CLT) [2]. The case studied is a $(0/45/90/-45)_s$ quasi-isotropic laminate (1 in. wide by 2 in. long) subjected to thermal loads. The mesh pattern used in the finite element solution consists of 50 4-node square elements with a total of 132 degrees of freedom (Fig. 3a). The compliance function $S_{22}(t)$ and $S_{66}(t)$ at $T = 75°F$ are given below:

$$S_{22} = 0.7143 \times 10^{-6} + 0.00385 \times 10^{-6} \, t^{0.33} \ (\text{psi})^{-1}$$
$$S_{66} = 1.1111 \times 10^{-6} + 0.00680 \times 10^{-6} \, t^{0.31} \ (\text{psi})^{-1}$$

where t is in minutes. Other constants are assumed to be independent of time, i.e. E_{11} = 18 x 10^6 psi and ν_{12}= 0.34. The normalized master curves $Q_{22}(t)$ represented by the exponential series and the power law are illustrated in Fig. 4.

Using these material properties the stress and strain histories have been calculated for two loading conditions. Case I involves an instantaneous change of temperature from 350°F to 75°F at time t = 0 with the temperature held at 75°F thereafter. Case II is a sudden temperature change from 350°F to 160°F at t = 0 with the temperature kept at 160°F afterwards. The in-plane strains ε_x obtained for Case I are shown in Fig. 5. It is seen that the present finite element solution agrees well with the incremental solution from the CLT approach, the maximum discrepancy being 1.5%. Note that the strain ε_x decreases with time. After 1.2096 x 10^6 seconds (two weeks), the magnitude of the strain decreases by 10.5% in Case I (ΔT = -275° F and T = 75°) and 42.7% in Case II (ΔT = -190° F and T = 160°F). The viscoelastic stress σ_x in the 0° layer of the $(0/45/90/-45)_s$ laminate, normalized with respect to the initial thermal stress at time t = 0, is shown in Fig. 6 for both cases of loading. The initial thermal stress $\sigma_x(0)$ in the 0° layer is -5380 psi for ΔT = -275°F (Case I) and -3717 psi for ΔT = -190°F (Case II). It is noted that while the elastic solution is linearly proportional to the temperature change, the stress in a viscoelastic analysis relaxes with time in different proportions (see Fig. 6); at the completion of 336 hours the thermal stress σ_x relaxes 11.9% in Case I loading and 48.4% in Case II. The difference in the amount of stress relaxed is due to the fact that relaxation moduli $\overline{Q}_{ij}$ depend on both the current temperature and time. The relaxation moduli decrease more significantly with time at the higher temperature (T = 160°F, Case II) than at the lower temperature (T = 75°F, Case I). Comparison of these results also

shows the nonlinear effect of temperature on stress relaxation.

Figure 7 depicts the laminate strain history normalized with respect to the initial strain at time t = 0. The initial strain values are ε_x = -4.56 x 10^{-4} in/in for Case I loading and ε_x = -3.15 x 10^{-4} in/in for Case II. It is interesting to note that in both cases the magnitude of laminate strain ε_x decreases rather than increases with time. After t = 1.2E6 sec. (two weeks) the magnitude of laminate strain in Case I (ΔT = -275°F and T_0 = 75°F) decreases 10.5%, while the laminate strain in Case II (ΔT = -190°F and T_0 = 160°F) decreases 42.7%.

The effects of different temperature spectrums on stress relaxation and creep strains for $(45/-45)_s$ graphite/epoxy laminates were also investigated. Two conceivable temperature histories are shown in Fig. 8. The dotted line (Path A) in the figure denotes that the laminate is cooled down slowly in a stepwise fashion from T = 350°F at t = 0 to room temperature T = 75°F at t = 98 days. The temperature variations are composed of a series of elastic steps (Δt = 0) and isothermal processes (constant temperature). The solid line (Path B) indicates that the laminate is cooled down suddenly from T = 350°F to room temperature at t = 0, after which it is subjected to a cyclic temperature variation. The residual stresses and strains in the 45° layer associated with these two temperature histories are presented in Fig. 9 and Fig. 10, respectively. Although the laminate eventually reaches the same temperature (75°F) after 98 days, the residual thermal stress and strain are much greater in magnitude for the cyclic temperature history (Path B). The sum of thermal stresses induced during all elastic step changes of temperature (Δt = 0) is equal to the elastic thermal stress due to the net temperature change from the stress-free temperature (350°F) to room temperature (75°F). That is, in the

13

Path A spectrum the sum of stresses τ_{xy} shown by $OA_1 + A_2A_3 + A_4A_5 + A_6A_7 + A_8A_9 + A_{10}A_{11} + A_{12}A_{13}$ is equal to the stress τ_{xy} denoted by OB_1. In Path B loading, the amount of stress τ_{xy} represented by $OB_1 - B_2B_3 + B_4B_5 - B_6B_7 + B_8B_9 - B_{10}B_{11} + B_{12}B_{13}$ is equal to OB_1. However, the temperatures at which the stress relaxation occurs are different. At high temperature the rate of stress relaxation is high, hence the laminate undergoes more relaxation in Path A spectrum. For example, during the first time interval the stress τ_{xy} relaxes from A_1 to A_2 in Path A spectrum while τ_{xy} relaxes a smaller amount from B_1 to B_2 in the Path B spectrum. Thus, the stress histories depend strongly on the specific load spectrum applied.

Another example considered is the time-dependent response of a symmetric laminate at room temperature (75°F) when subjected to mechanical loads. The history of mechanical loading is plotted in Fig. 11. The average stress applied is equal to 1,728 psi initially and is held constant until t = 24 hours, after which the laminate is unloaded elastically. The creep and recovery behavior for the three different laminates, $(0/90)_s$, $(45/-45)_s$, and $(0/45/90/-45)_s$ layups, are plotted in Fig. 12. As expected, the $(45/-45)_s$ layup exhibits the most significant creep response among these three laminates. The initial in-plane strains ϵ_x along the loading direction are equal to 0.564×10^{-3} for the $(45/-45)_s$ laminate, 0.24×10^{-3} for the $(0/45/90/-45)_s$ laminate and 0.177×10^{-3} for the $(0/90)_s$ laminate. After 24 hours the strain ϵ_x increases by 10.75% in $(45/-45)_s$ laminate, 1.16% in the $(0/45/90/-45)_s$ laminate and 0.5% in the $(0/90)_s$ laminate. When the load is released in the elastic step ($\Delta t = 0$) at t = 24 hours the strain ϵ_x is suddenly reduced to 0.607×10^{-4} in the $(45/-45)_s$ laminate, to 0.279×10^{-5} in the $(0/45/90/-45)_s$ laminate and to 0.849×10^{-6} in the $(0/90)_s$ laminate. Note that the creep recovery rate of the $(45/-45)_s$ laminate is also much higher

14

than the other two laminates.

It must be noted that a sufficiently small time interval is usually required in order to obtain accurate solutions to Eq. (22). The number of time steps needed generally depends on the shape of the applied load spectrum and more time steps are required for a complex load history. A criterion used for choosing the proper time step size is to compare the creep response of a unidirectional laminate due to a unit step stress with the time variation of the components in the compliance matrix. For instance, if a unit step stress σ_x is applied the resulting creep strain $\varepsilon_x(t)$ must be equal to the compliance component $\bar{S}_{11}(t)$. In all of the above analyses, 12 time steps with variable interval Δt were used. Typically the Δt value is set to 100 sec. at t = 0 and increases with time to a maximum of 4.3×10^4 seconds.

5.2 Notched Composites

The geometry considered for a notched composite is a 1 in. wide by 2 in. long laminate with a circular hole of diameter 0.25 in. at the center. Since there are no viscoelastic solutions available for comparison with this case, the accuracy of the finite element solution is estimated based on the elastic results at time t = 0. To compare the elastic solutions, three finite element mesh geometries were used. The resulting elastic stress concentration factors are given in Table 4. All three solutions compare well with the solution by Nuismer and Whitney [10], indicating the adequacy of the mesh geometry. As a result (of this congruity) an intermediate mesh pattern with 670 degrees of freedom is used for the following viscoelastic analysis (see Fig. 3b for mesh geometry).

A uniform stress of σ_x = 20,000 psi is applied at the remote boundary of

15

the laminate at a constant temperature of 122° F. Any residual thermal stress which may exist in the laminate at the completion of the curing process is neglected. The in-plane circumferential strains ε_ϕ at the hole edge are plotted in Fig. 13 as a function of ϕ for the $(45/0/-45/90)_s$ laminate over a time period of 10^8 seconds. Similar results are shown in Fig. 14 for a $(45/-45)_s$ laminate. In both cases, the magnitude of the circumferential strains ε_ϕ increases with time. At $t = 0$, the circumferential strain ε_ϕ at ϕ = 90° is 0.897 x 10^{-2} for the $(0/45/90/-45)_s$ laminate and 0.155 x 10^{-1} for the $(45/-45)_s$ laminate. As expected the strain ε_ϕ in the $(45/-45)$ layup increases at a much higher rate (51.3%) than the strain in the quasi-isotropic laminate.

The relaxation of stresses in graphite/epoxy laminates subjected to a uniform strain ε_x = 0.003 in./in. is also studied. The stress averaged through the thickness is obtained as a function of time. The average circumferential stress σ_ϕ is shown in Fig. 15 for a $(45/0/-45/90)_s$ laminate and in Fig. 16 for a $(45/-45)_s$ laminate. In the $(45/0/-45/90)_s$ laminate, the maximum circumferential stress σ_ϕ occurs at ϕ = 90°. This stress decreases from an initial value of 65328 psi to 63584 psi at $t = 10^5$ sec. to 61205 psi after 10^8 seconds. In the $(45/-45)_s$ layup, the stress distribution is somewhat different from the quasi-isotropic case as can be seen in Fig. 16. For the $(45/-45)_s$ laminate the maximum circumferential stress occurs at about ϕ = 60° rather than ϕ = 90°. At ϕ = 60°, the stress σ_ϕ relaxes from a maximum value of 27271 psi to 24102 psi after 10^5 seconds and eventually to 19472 psi after 10^8 seconds. Additionally, the location of the maximum stress concentration moves slightly from ϕ = 60° as time elapses. As before, the $(45/-45)_s$ laminate exhibits a much higher stress relaxation rate than the quasi-isotropic layup.

5.3 Three-Dimensional Viscoelastic Results

A. Verification Studies

Since there is no 3-D viscoelastic solution available for a laminate with a circular hole, the two verification studies are limited to elastic case. In the first study, a 2 in. by 2 in. by 0.1 in. thick isotropic plate with a circular hole of 0.25 in. in diameter is analyzed. A uniform stress σ_x of 1 psi is applied along the boundary at x = ± 1 in. The material properties are $E = 30 \times 10^6$ psi and $\nu = 0.336$. The finite element mesh pattern used has 10 (ϕ-direction) by 9 (r-direction) by 6 (z-direction) mesh divisions with a total of 2310 degrees of freedom. The resulting circumferential stresses σ_ϕ at z = 0.025 in. are plotted in Figure 17. Also shown in the figure are the corresponding 2-D results. It is seen that these two solutions are in good agreement with the maximum error being 3% at $\phi = 90°$.

The second study analyzes a $(90/0)_s$ boron/epoxy laminate with a circular hole in the center. The plate dimensions and the finite element mesh geometry are identical with those shown for the isotropic plate. In order to compare the solution material properties given in [11] are used. A uniaxial average stress σ_x of 1 psi is applied at a remote boundary. The resulting in-plane tangential stresses in the 0° ply are shown in Fig. 18 along with those obtained in [11-13]. The stresses in the 90° ply are also shown in Fig. 19. Good agreement between the present and the other solutions is observed. Fig. 20 compares the normal stress σ_z in the mid-plane from various solutions [11,13,14]. On a relative basis, there are more discrepancies in the σ_z stress distribution than the σ_ϕ stress among these solutions. Higher stresses are obtained in [11] by the use of special hybrid elements around a circular hole. On the other hand, the solution in [13] uses a boundary layer method

and is significantly different from others [11,12] near $\phi = 90°$. In any case, some experimental studies remain to be done in order to verify the accuracy of the 3-D analytical results.

B. Viscoelastic Response of Cross-Ply Laminates

The time-dependent 3-D stresses around a circular hole in graphite/epoxy $(0/90)_s$ and $(90/0)_s$ laminates are analyzed. A uniform displacement of $u_x = 0.005$ in is prescribed along the remote boundary $x = \pm 1.0$ in. Due to symmetry, only one-eighth of the laminate is considered in the analysis. As shown in Fig. 21, this model contains 440 3-D solid elements with 2010 degrees of freedom. The material properties given in Table 1 are used. The viscoelastic response in the 140°F environment is investigated over a time period up to 1 year (3.15×10^7 seconds). The distributions of interlaminar normal and shear stresses around the hole edge are obtained as a function of time.

Fig. 22 shows the normal stress σ_z around a hole in the midplane ($z = 0$) of the $(0/90)_s$ laminate. The maximum σ_z which occurs approximately at $\phi = 36°$ relaxes by 28% after one year. For the $(90/0)_s$ laminate the σ_z distributions are completely different as shown in Fig. 23; the maximum stress in the $(90/0)_s$ layup occurs at $\phi = 90°$. Furthermore, the magnitude of σ_z in the $(90/0)_s$ is one order higher than that of the $(0/90)_s$ laminate. Thus, the normal σ_z stress is strongly dependent on the laminate stacking sequence.

The interlaminar normal stress at the interface ($z/h = 1.0$) of the $(0/90)_s$ laminate is shown in Fig. 24. For an applied strain of 0.005 in/in, the maximum elastic stress σ_z at the 0/90 interface is about 3700 psi which is close to 75% of the static ultimate strength of a matrix material. As a

result, delamination at this interface is expected to occur as the loading is increased. The σ_z distribution at the interface in the $(90/0)_s$ layup is shown in Fig. 25. In the $(90/0)_s$ layup the interface stress σ_z is also large but it is smaller than the corresponding midplane stress. In both $(0/90)_s$ and $(90/0)_s$ laminates, the interlaminar stress σ_z is in tension and can cause delaminations between plies.

The interlaminar shear stresses $\tau_{z\phi}$ at the interface in both $(0/90)s$ and $(90/0)s$ laminates are shown in Figs. 26 and 27. Approximately opposite distributions are observed for the interlaminar shear stress in these two laminates.

The effects of time and temperature on the stress relaxation in a cross-ply laminate is illustrated in Fig. 28. The maximum interlaminar normal stress at $\phi = 90°$ in the $(0/90)_s$ laminate is plotted as a function of time at 70°F and 140°F. In this figure, the stress σ_z has been normalized with respect to its elastic solution at time $t = 0$. Similar curves are shown in Fig. 29 for the $(90/0)$ laminate. After 1 year the maximum stress relaxes 48% in the $(0/90)_s$ laminate and 37% in the $(90/0)_s$ laminate. The normalized interlaminar shear stress at $\phi = 54°$ is shown in Fig. 30. Less relaxation is observed for the $\tau_{z\phi}$ stress than for the σ_z stress.

C. $(45/-45)_s$ Laminates

In $(45/-45)_s$ laminates the conditions of symmetry used for the $(0/90)s$ layup are no longer valid. However, other symmetric and antisymmetric conditions in displacements and stresses can be utilized so that only a quarter of the plate is sufficient for the analysis [15]. Fig. 31 shows a typical finite element model for the $(45/-45)_s$ laminate which has 512 solid

elements with 2310 degrees of freedom. The boundary conditions and material properties are the same as those used for a $(0/90)_s$ laminate.

The normal stress σ_z at the midplane is shown in Fig. 32 for $T = 140°F$. It is noted that the σ_z is distributed between a tensile stress of 4750 psi and a compressive stress of 4200 psi with the maximum stress occuring at $\phi = 78.8°$. At $\phi = 33.8°$ and $-56.2°$ the stress values appear to be independent of time. Fig. 33 illustrates the interlaminar shear stress distribution at the 45/-45 interface. For the applied strain of 0.005 in/in the maximum value of $\tau_{z\phi}$ at $\phi = 90°$ is 8840 psi which is large enough to initiate delamination. The inplane circumferential stress in the $-45°$ ply is shown in Fig. 34. As can be seen in these figures the $(45/-45)_s$ layup exhibits much stronger viscoelastic effect than a cross-ply laminate.

D. Quasi-isotropic Laminates

Three-dimensional analyses are also performed for a quasi-isotropic $(45/0/-45/90)_s$ laminate with a circular hole at $T = 140°F$. A quarter of the laminate including 1025 elements and 4158 degrees of freedom is used in the analysis. The finite element mesh pattern used is similar to that shown in Fig. 31 except there are 8 subdivisions in the thickness (z) directions. An average σ_x-stress of 1 psi is applied to the laminate edges $x = \pm 1$ in. This condition results in a σ_x of 2.296 psi, 0.763 psi, and 0.178 psi in the 0, 45 (or -45) and 90 plys, respectively. These ply stresses are used as boundary conditions for the problem.

The circumferential strains ε_ϕ around the hole ($r/a = 1.04$) in each ply are shown in Fig. 35. The ply strain is also compared with the 2-D results from Section 5.2. The strain ε_ϕ is fairly uniform throughout the laminate

thickness. The time-dependence of the ε_ϕ strain in the 90° layer is shown in Fig. 36. A maximum of 14.6% increase in ε_ϕ is obtained after one year. It is interesting to note that the ε_ϕ distribution in each layer is almost symmetric about the centerline $\phi = 0$. This suggests that additional symmetry conditions can be imposed in the finite element model, i.e. only one eighth of the laminate is sufficient for the calculation of ε_ϕ in a quasi-isotropic laminate.

The transverse strain ε_z distributions are plotted in Fig. 37 for the 90-ply (z/h = 0.75) and in Fig. 38 for the 0-ply (z/h = 2.75). These distributions are quite different from the ε_ϕ results; the transverse strain ε_z is not symmetric with respect to $\phi = 0$. Furthermore, the amount of strain increase in the 0-ply is relatively large. An explanation for this behavior is that during creep the 45 and 90 plies lose stiffness since the material properties degrade most in these layers. This yields much higher strains in the 45 and 90 plies than in the 0-ply. However, due to the compatibility condition between adjacent layers additional interlaminar shear stresses are built up and are added to the 0-ply. As a result, the actual loads increase in the 0-ply during creep resulting in a much larger strain than would be obtained for a unidirectional composite. This load transferring mechanism is illustrated in Fig. 39 in which the in-plane stress σ_x near the remote boundary x = 1.0 is shown at two different times. The σ_x stress increases 10% in the 0-ply but decreases 15.6% in the 45-ply and 32% in the 90-ply after one year.

Figure 40 depicts the interlaminar shear strain $\gamma_{z\phi}$ in the -45 ply around a circular hole. This distribution is a mirror image of that in the +45 ply. Over a period of one year the rate of increase in shear strain is 60% at

21

ϕ = +62° in the -45° ply. The high creep strain rate is due to the fact that the GY70/339 material used in the analysis has strong time-dependent properties.

E. Matrix Dominated Laminates

The last example analyzed is a $(90/-45/90-45)_s$ laminate whose properties are dominated by the matrix material. The boundary conditions applied are σ_x = 0.389 psi in the 90-ply and σ_x = 1.621 psi in both 45 and -45 plies. These conditions yield an average stress σ_x of 1 psi across the laminate thickness.

Results of strains ε_ϕ in each ply of the $(90/-45/90-45)_s$ laminate at T = 140°F are compared with the corresponding 2-D solution in Fig. 41. The strain component ε_ϕ, ε_z, and $\gamma_{\phi z}$ in the 90 layer (z/h = 3.75) are plotted in Figs. 42, 43, and 44, respectively. As expected, much higher creep rate is observed in a matrix dominated layup than in a quasi-isotropic laminate. Specifically, the maximum strain ε_ϕ increases 50% in the $(90/-45/90/45)$s layup as compared to 14.6% in the $(45/0/-45/90)$s layup over a time period of one year. As before, such a large creep rate is due to the material properties assumed in the analysis.

6. CONCLUSION

The time dependent behavior of composite materials has been described by an anisotropic thermo-viscoelastic constitutive model. A numerical procedure has been developed for the solution of time-dependent stresses and strains in composite laminates containing geometric discontinuities and complicated boundary conditions. Using this procedure, the stress and strain distributions around a circular hole in graphite/epoxy composites have been obtained as a function of time for both mechanical and thermal loads. The effects of layup orientation and load spectrum on deformation histories have been demonstrated. The results show that the present method gives the accurate and efficient numerical solutions of complex anisotropic thermoviscoelastic boundary value problems.

REFERENCES

1. Elber, W., and Guynn, E.G., NASA Langley Research Center, Private Communication.

2. Tuttle, M.E., and Brinson, H.F., "Prediction of the Long-Term Creep Compliance of General Composite Laminates," Experimental Mechanics, Vol. 26 (1), March 1986.

3. Flaggs, D.L., and Crossman, F.W., "Analysis of the Viscoelastic Response of Composite Laminates During Hygrothermal Exposure," J. of Composite Materials, Vol. 15, January 1981, p. 21.

4. Harper, B.D., and Weitsman, Y., "On the Effects of Environmental Conditioning on Residual Stresses in Composite Laminates," Int. J. Solids Structures, Vol. 21, 1985, p. 907.

5. Shapery, R.A., "Stress Analysis of Viscoelastic Composite Materials," J. of Composite Materials, Vol. 1, January 1967, p. 228.

6. Christensen, R.M., Theory of Viscoelasticity, Academic Press, New York, 1982.

7. Taylor, R.L., Pister, K.S., and Goudreau, G.L., "Thermomechanical Analysis of Viscoelastic Solids," Int. J. for Numerical Methods in Eng., Vol. 2, 1970, p. 45.

8. Flaggs, D.L., ADVLAM (An Advanced Composite Laminate Analysis Code) User's Manual, Lockheed Palo Alto Research Lab., September 1983.

9. Yeow, Y.T., Morris, D.H., and Brinson, H.F., "Time-Temperature Behavior of a Unidirectional Graphite/Epoxy Composite," ASTM STP 674, 1979, p. 263.

10. Nuismer, R.J., and Whitney, J.M., "Uniaxial Failure of Composite Laminates Containing Stress Concentrations," Fracture Mechanics of Composites, ASTM STP 593, 1975, p. 117.

11. Nishioka, T. and Atluri, S.N., "Stress Analysis of Holes in Angle-ply Laminates: an Efficient Assumed Stress "Special-Hole-Element" Approach and a Simple Estimation Method," Computers & Structures, Vol. 15, 1982, p. 135.

12. Rybicki, E.F. and Hopper, A.T., "Analytical Investigation of Stress Concentrations Due to Holes in Fiber Reinforced Plastic Laminated Plates: Three-Dimensional Models," AFML-TR-73-100, Battelle Columbus Labs, 1973.

13. Tang, S., "A Variational Approach to Edge Stress of Circular Cutouts in Composites," AIAA paper 79-0802, 20th AIAA/ASME/ASCE/AHS, SMD Conf., St. Louis, MO, 1979, p. 326.

14. Rybicki, E.F. and Schmuesser, D.W., "Three-dimensional Finite Element Stress Analysis of Laminated Plates Containing a Circular Hole," AFML-TR-76-92, Battelle Columbus Labs, 1976.

15. Lee, J.D., "Three Dimensional Finite Element Analysis of Damage Accumulation in Composite Laminate," Computers & Structures, Vol. 15, 1982, p. 335.

APPENDIX A

1. For the two dimensional analysis,

$$Q_1 = Q_{11}, \quad Q_2 = Q_{22}, \quad Q_3 = Q_{12}, \quad Q_4 = Q_{66},$$

and

$$n_{111} = m^4, \quad n_{112} = n^4, \quad n_{113} = 2\,m^2n^2, \quad n_{114} = 4\,m^2n^2$$

$$n_{121} = m^2n^2, \quad n_{122} = m^2n^2, \quad n_{123} = m^4 + n^4, \quad n_{124} = -4\,m^2n^2$$

$$n_{131} = m^3n, \quad n_{132} = -mn^3, \quad n_{133} = mn\,(n^2 - m^2), \quad n_{134} = 2\,mn\,(n^2 - m^2)$$

$$n_{221} = n^4, \quad n_{222} = m^4, \quad n_{223} = 2\,m^2n^2, \quad n_{224} = 4\,m^2n^2$$

$$n_{231} = mn^3, \quad n_{232} = -m^3n, \quad n_{233} = mn\,(m^2 - n^2), \quad n_{234} = 2\,mn\,(m^2 - n^2)$$

$$n_{331} = m^2n^2, \quad n_{332} = m^2n^2, \quad n_{333} = -2\,m^2n^2, \quad n_{334} = (m^2 - n^2)^2$$

and all other $n_{ijr} = 0$ ($i,j = 1, 2, 3$, and $r = 1, 2, 3, 4$).

2. For the three-dimensional analysis,

$$n_{111} = m^4, \quad n_{112} = 2\,m^2n^2, \quad n_{114} = n^4, \quad n_{119} = 4\,m^2n^2$$

$$n_{121} = m^2n^2, \quad n_{122} = m^4 + n^4, \quad n_{124} = m^2n^2, \quad n_{129} = -4\,m^2n^2$$

$$n_{133} = m^2, \quad n_{135} = n^2, \quad n_{161} = m^3n, \quad n_{162} = -mn(m^2 - n^2)$$

$$n_{164} = -mn^3, \quad n_{169} = -2mn(m^2 - n^2), \quad n_{221} = n^4, \quad n_{222} = 2m^2n^2$$

$$n_{224} = m^4, \quad n_{229} = 4m^2n^2, \quad n_{233} = n^2, \quad n_{235} = m^2$$

$$n_{261} = n^3m, \quad n_{262} = mn(m^2 - n^2), \quad n_{264} = -m^3n, \quad n_{269} = 2mn(m^2 - n^2)$$

$$n_{336} = 1, \quad n_{363} = mn, \quad n_{365} = -mn, \quad n_{447} = m^2$$

$$n_{448} = n^2, \quad n_{457} = -mn, \quad n_{458} = mn, \quad n_{557} = n^2$$

$$n_{558} = m^2, \quad n_{661} = m^2n^2, \quad n_{662} = -2m^2n^2, \quad n_{664} = m^2n^2, \quad n_{669} = (m^2 - n^2)^2$$

and all other $n_{ijr} = 0$ ($i,j = 1, 2, \ldots 6$, and $r = 1, 2, \ldots 9$).

Table 1   Graphite/Epoxy Material Properties

Constant	Value
E_{11}	18×10^6 psi
E_{22}, E_{33}	1.4×10^6 psi
G_{12}, G_{13}, G_{23}	0.9×10^6 psi
ν_{12}, ν_{13}, ν_{23}	0.34
α_1	$0.2 \times 10^{-6}/°F$
α_2, α_3	$16.0 \times 10^{-6}/°F$

Table 2   Coefficients of Normalized Time-Varying Function
Used in the Viscoelastic Analysis

$$f(t) = f_0 + \sum_{i=1}^{10} f_i \exp(-t/\lambda_i)$$

i	f_i	λ_i
0	0.06698253	
1	0.0729459	8.174141919E+15
2	0.0696426	4.976486103E+14
3	0.150514	1.477467149E+13
4	0.148508	4.761315266E+11
5	0.146757	1.799163029E+10
6	0.102892	5.253922053E+08
7	0.114155	1.846670914E+07
8	0.071036	5.288067476E+05
9	0.0484272	1.494783951E+04
10	0.00813977	5.516602214E+02

Table 3   Shift Factors for Various Temperatures

Temperature (°F)	Shift Factor
75	1.0
104	8.9125
122	7.9433E+1
140	1.5849E+3
160	6.6069E+4
212	6.3096E+11
250	1.0000E+18

Table 4   Elastic Stress Concentration Factors (S.C.F.)

	Coarse Mesh	Intermediate Mesh	Fine Mesh	Ref. [10]*
S.C.F.	3.2470	3.2625	3.2514	3.2292
No. of Elements	110	297	570	
No. of DOF's	268	670	1246	

*The solution has been corrected for the finite width effect.
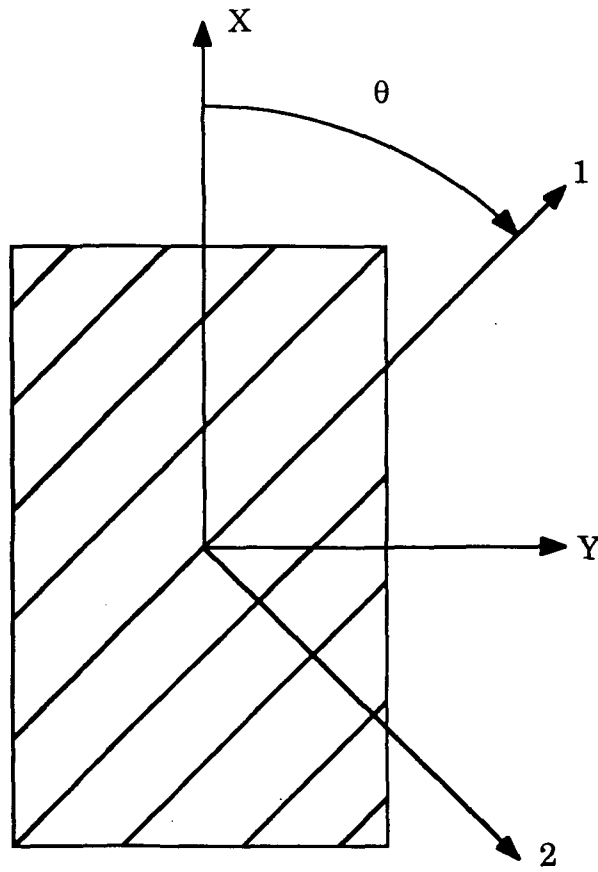
Fig. 1 Coordinate systems for a unidirectional composite
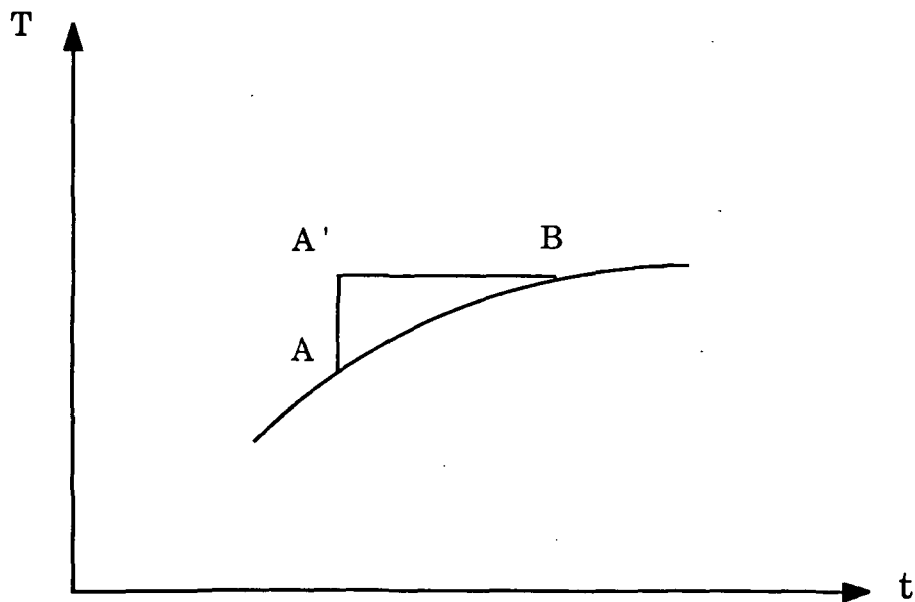
Fig. 2 Discretization of temperature history
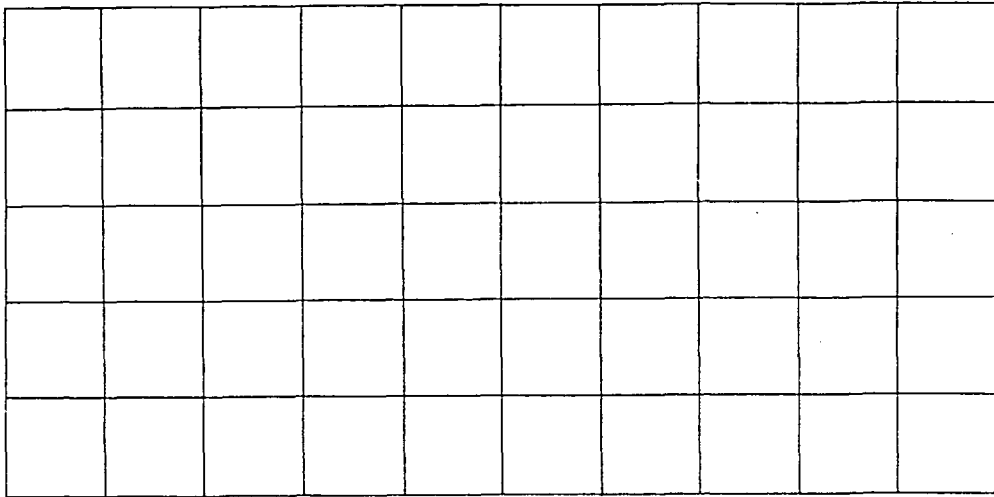
Fig. 3a Finite element mesh pattern for a unnotched laminate (2-D)
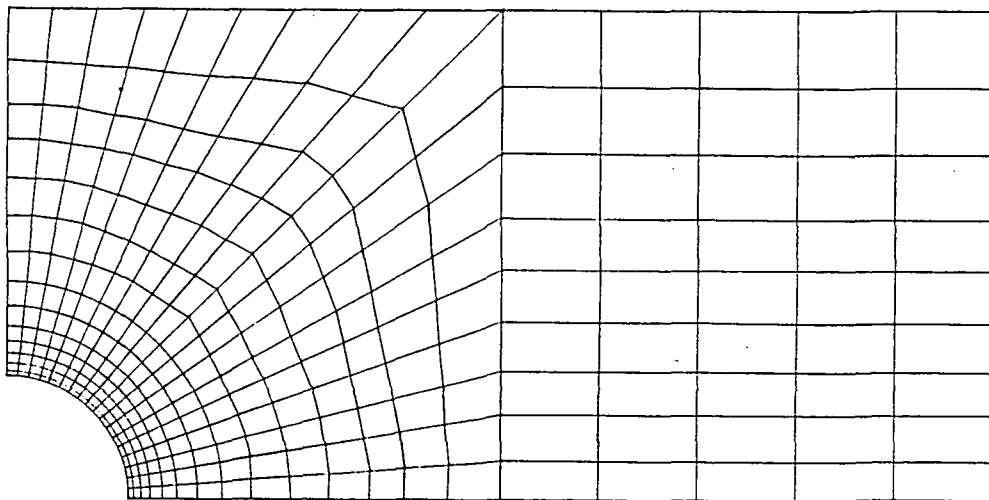
Fig. 3b Finite element mesh pattern for a notched laminate (2-D)
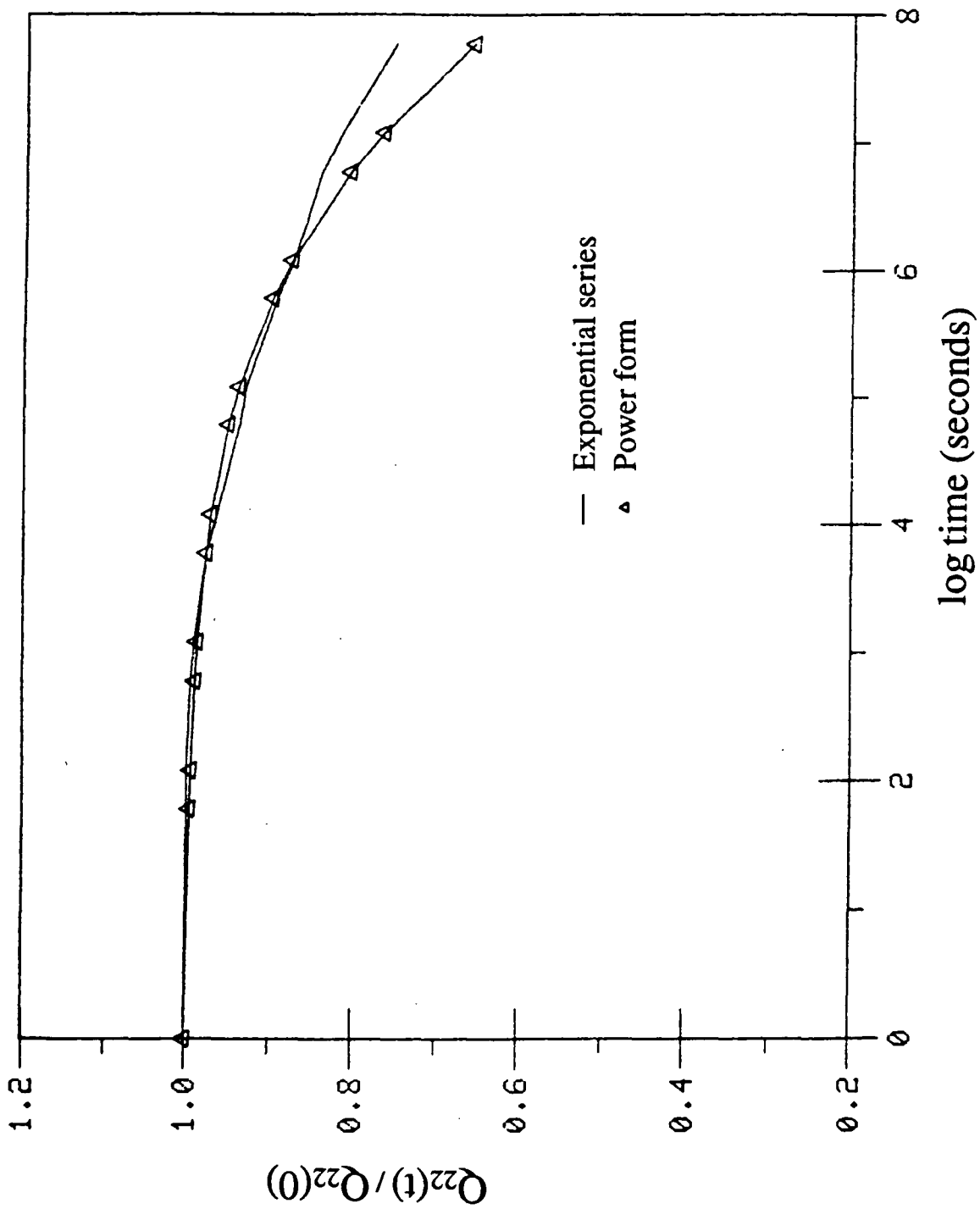
Fig. 4 Normalized relaxation function

Fig. 5 In-plane strains ε_x in a $(0/45/90/-45)_s$ laminate

$\varepsilon_x(0) = -4.56 \times 10^{-4}$

— Present
o CLT [Ref.2]
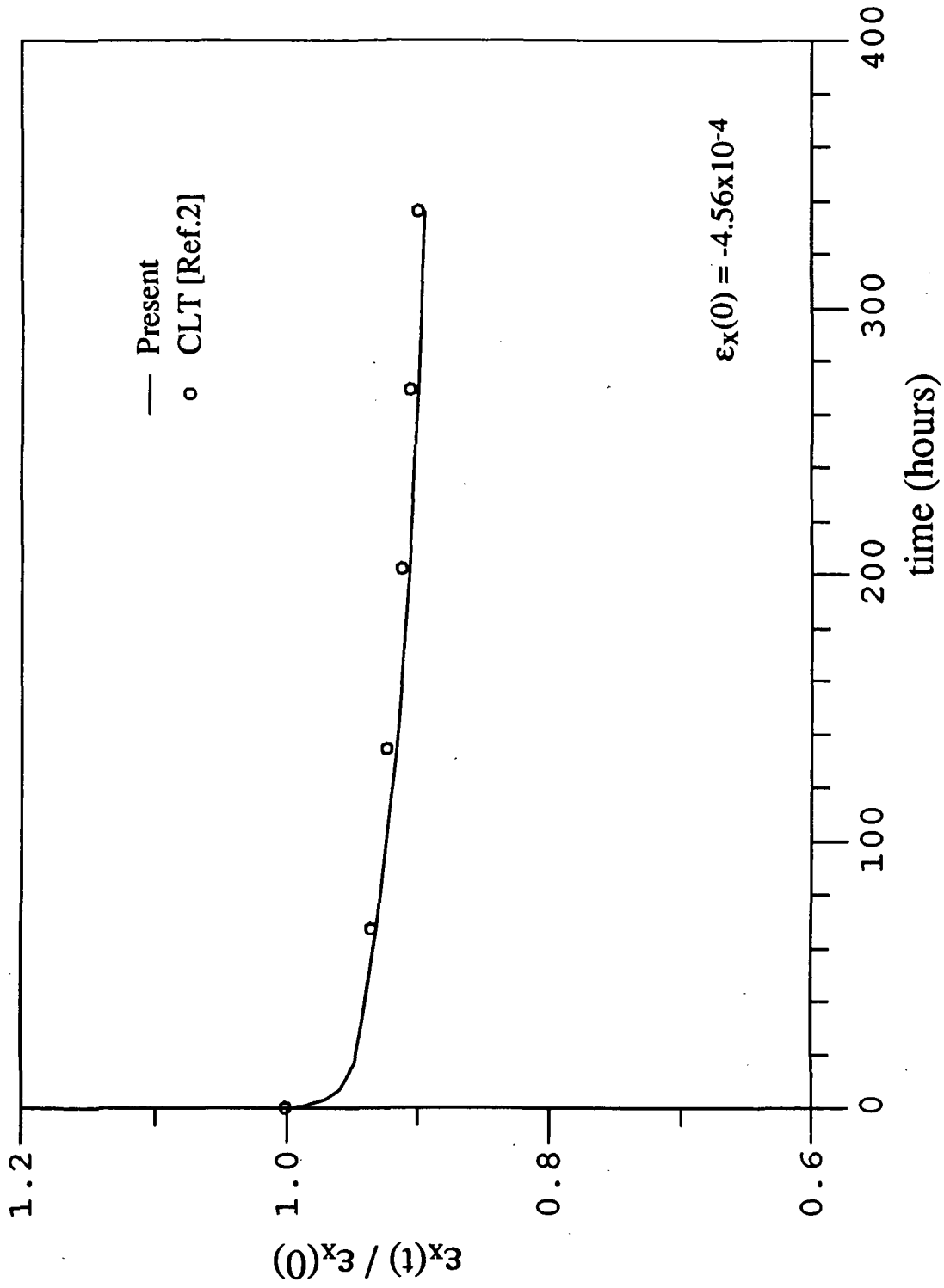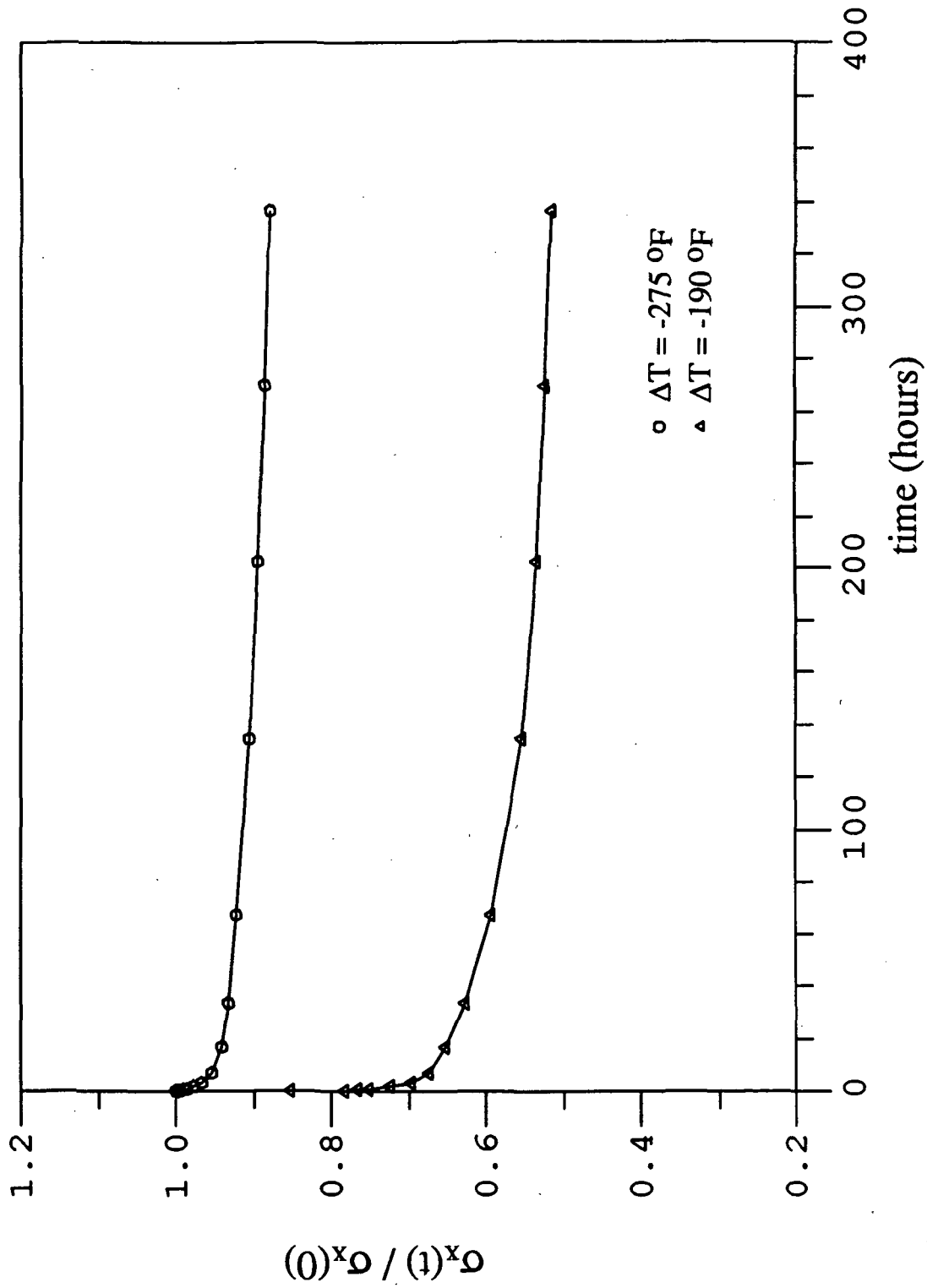
Fig. 6 Normalized thermal stresses σ_x in the 0° layer of a $(0/45/90/-45)_s$ laminate
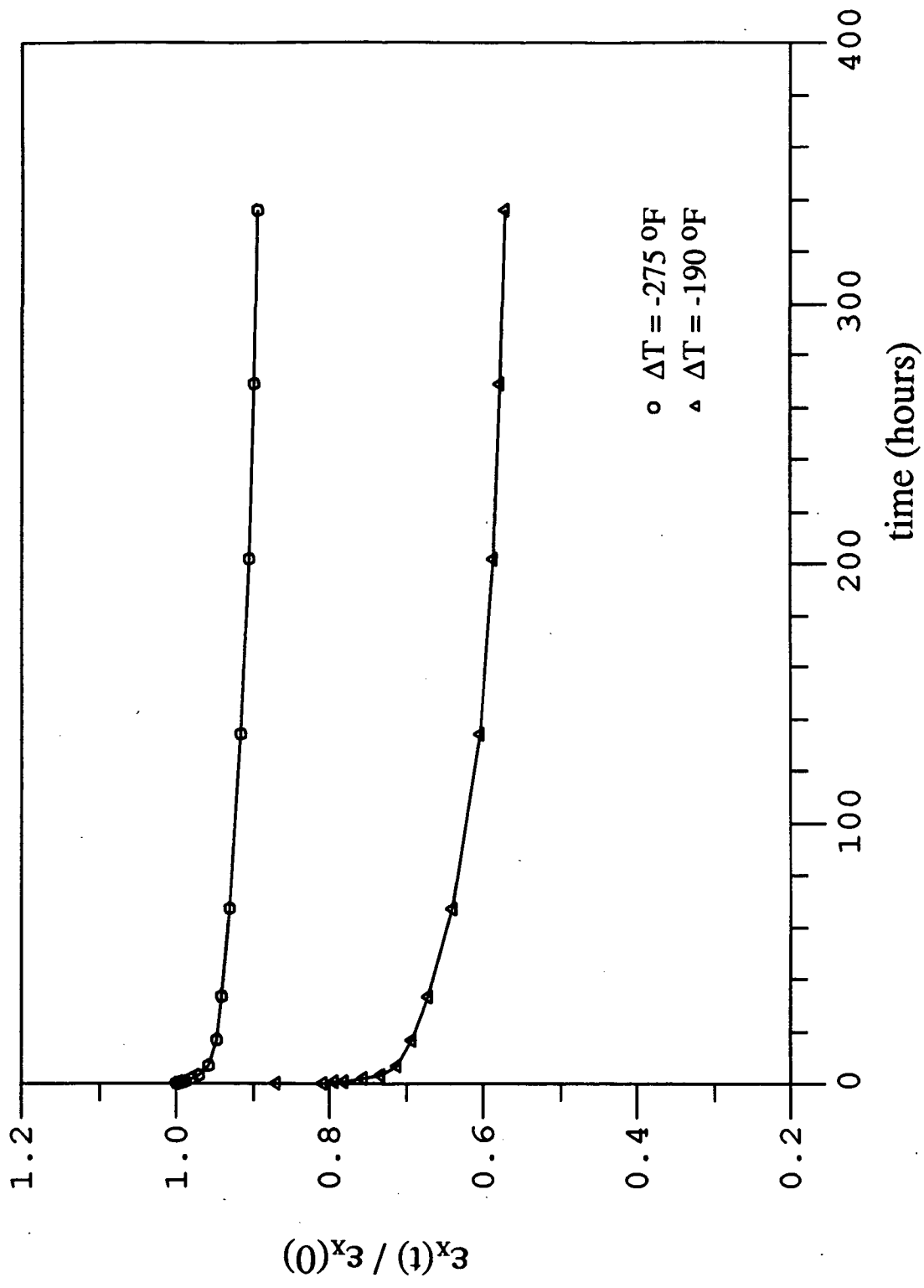
Fig. 7 Normalized in-plane strains ε_x for a $(0/45/90/-45)_s$ laminate

$\circ$ $\Delta T = -275\ ^\circ F$
$\triangle$ $\Delta T = -190\ ^\circ F$
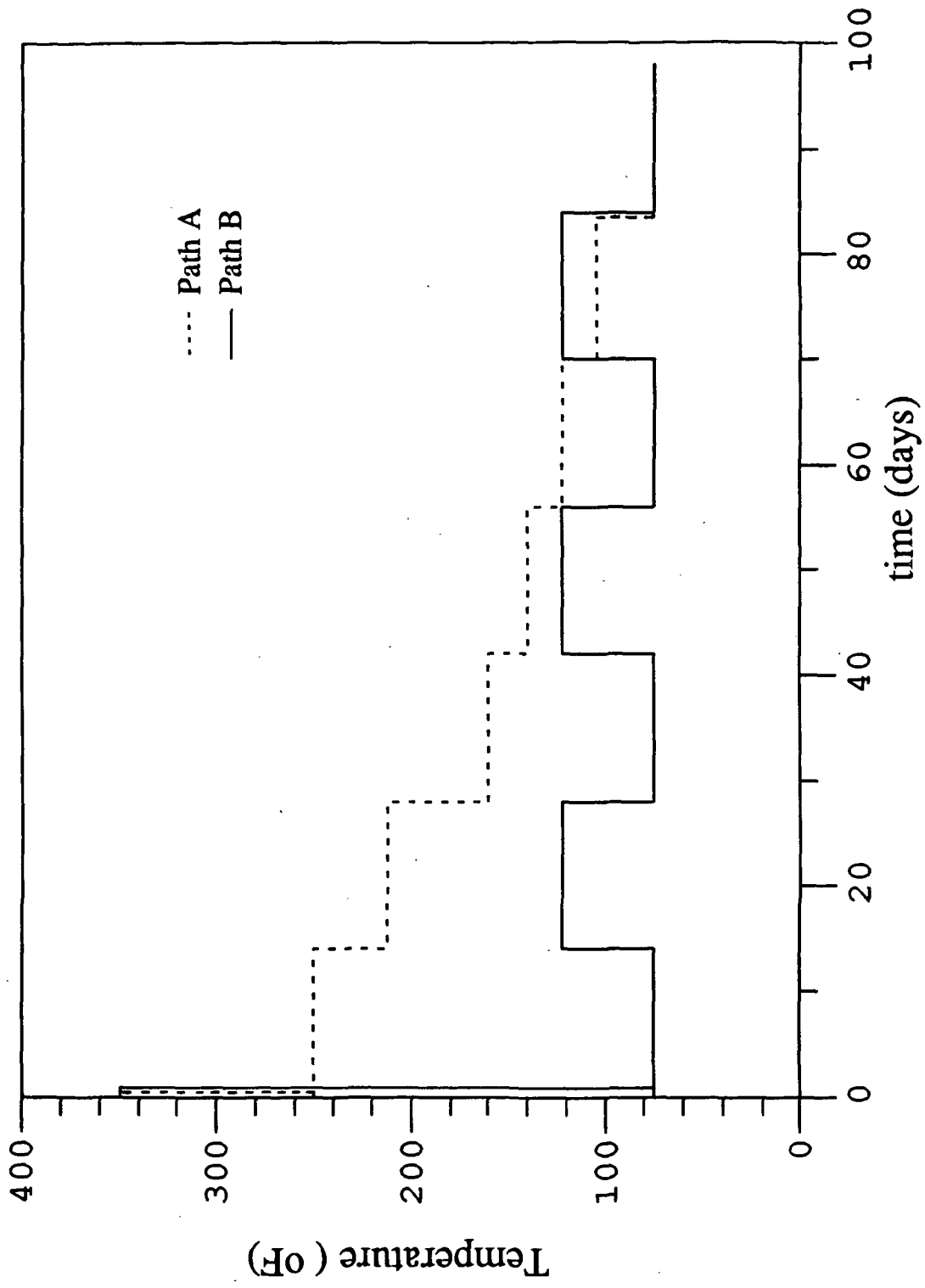
Fig. 8 Temperature history in a (45/-45)s laminate
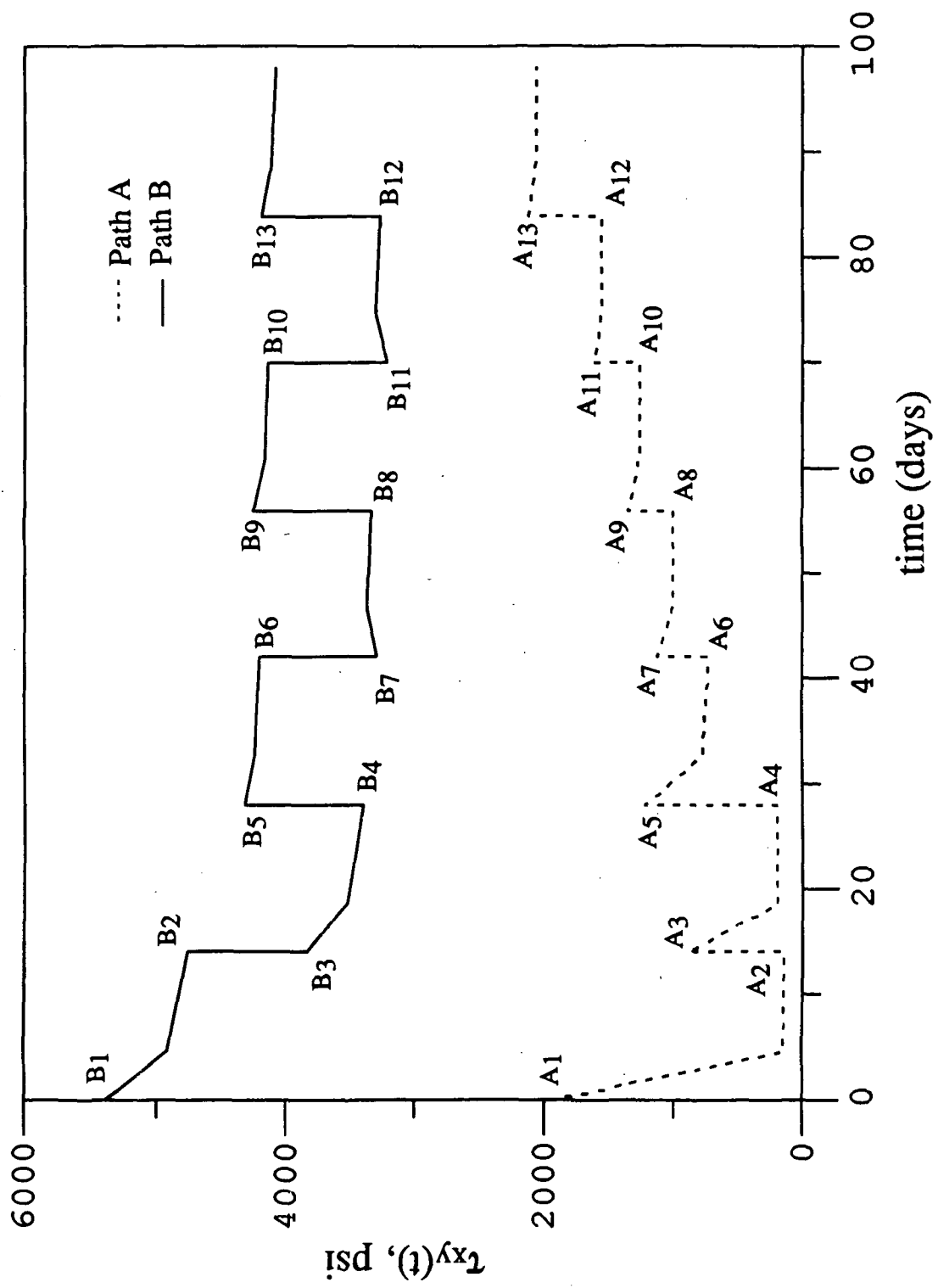
Fig. 9 Shear stresses τ_{xy} in the 45° layer of a (45/-45)$_s$ laminate
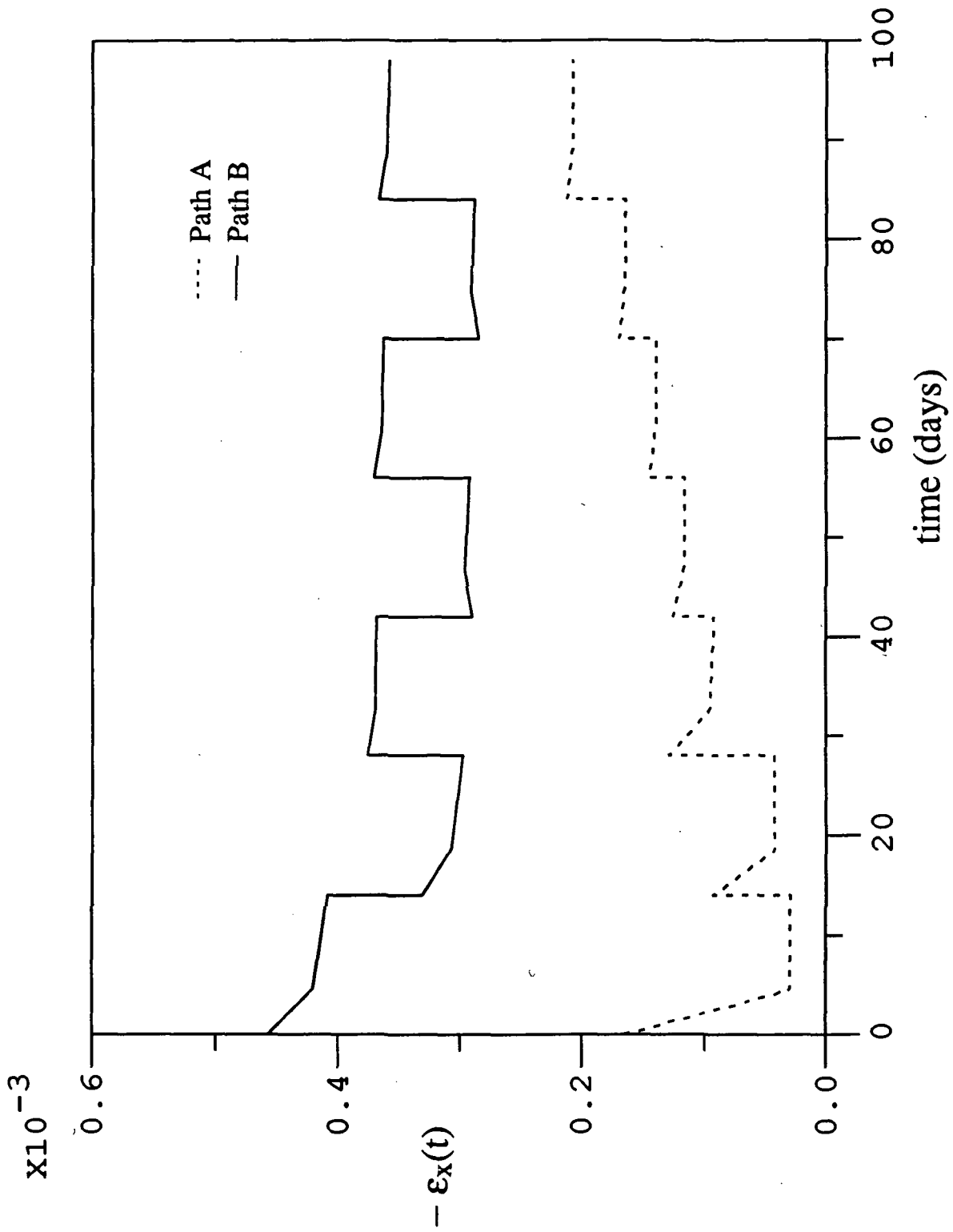
Fig. 10 In-plane strains ε_x in a (45/-45)s laminate
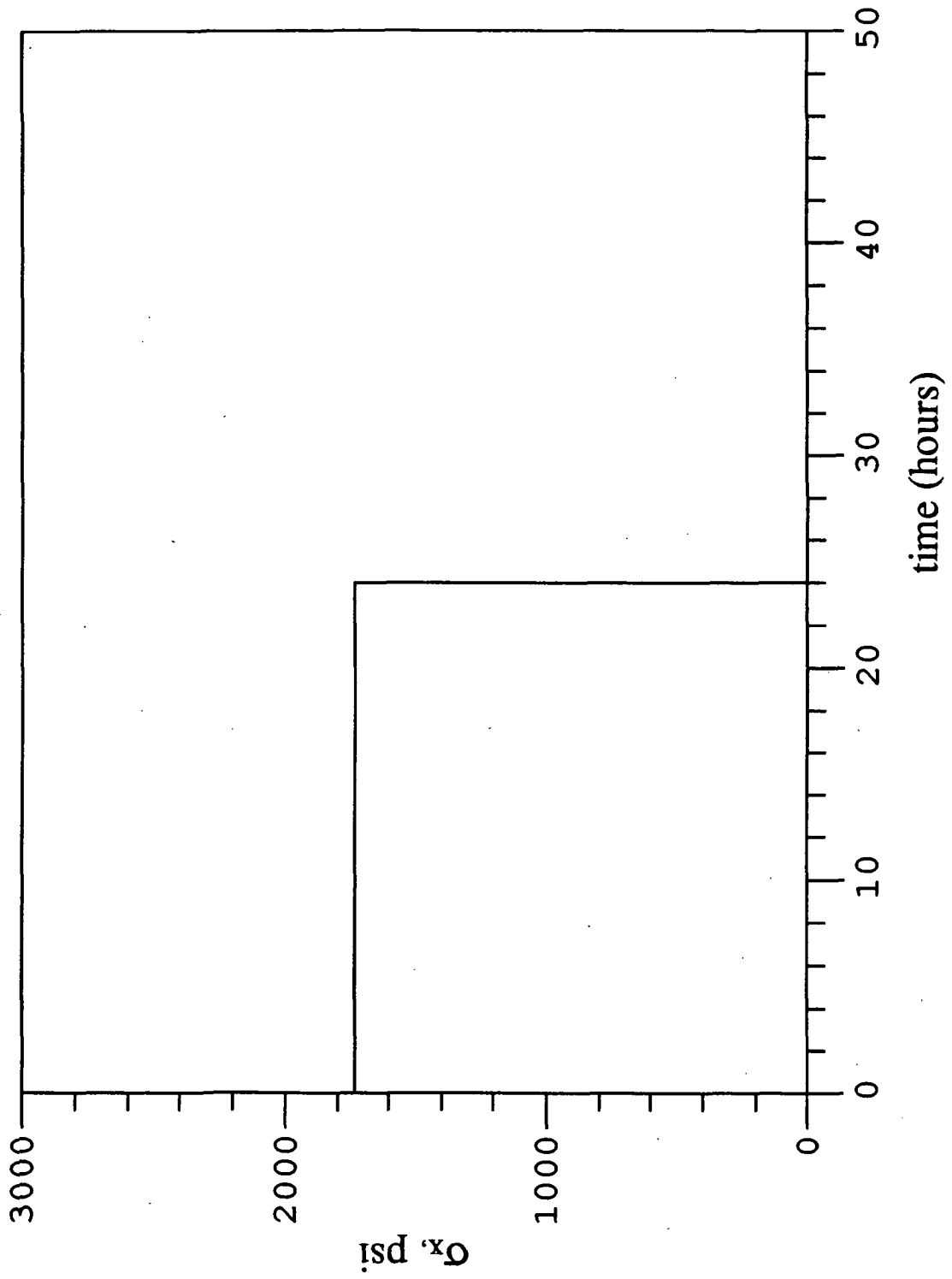
Fig. 11 Mechanical loading history

37

Fig. 12 In-plane strains ε_x in laminates

$\times 10^{-3}$

$\varepsilon_x(t)$

1.00

0.75

0.50

0.25

0.00

time (hours)

0   10   20   30   40   50

——— (45/-45)s

—·—· (0/45/90/-45)s

········ (0/90)s

38
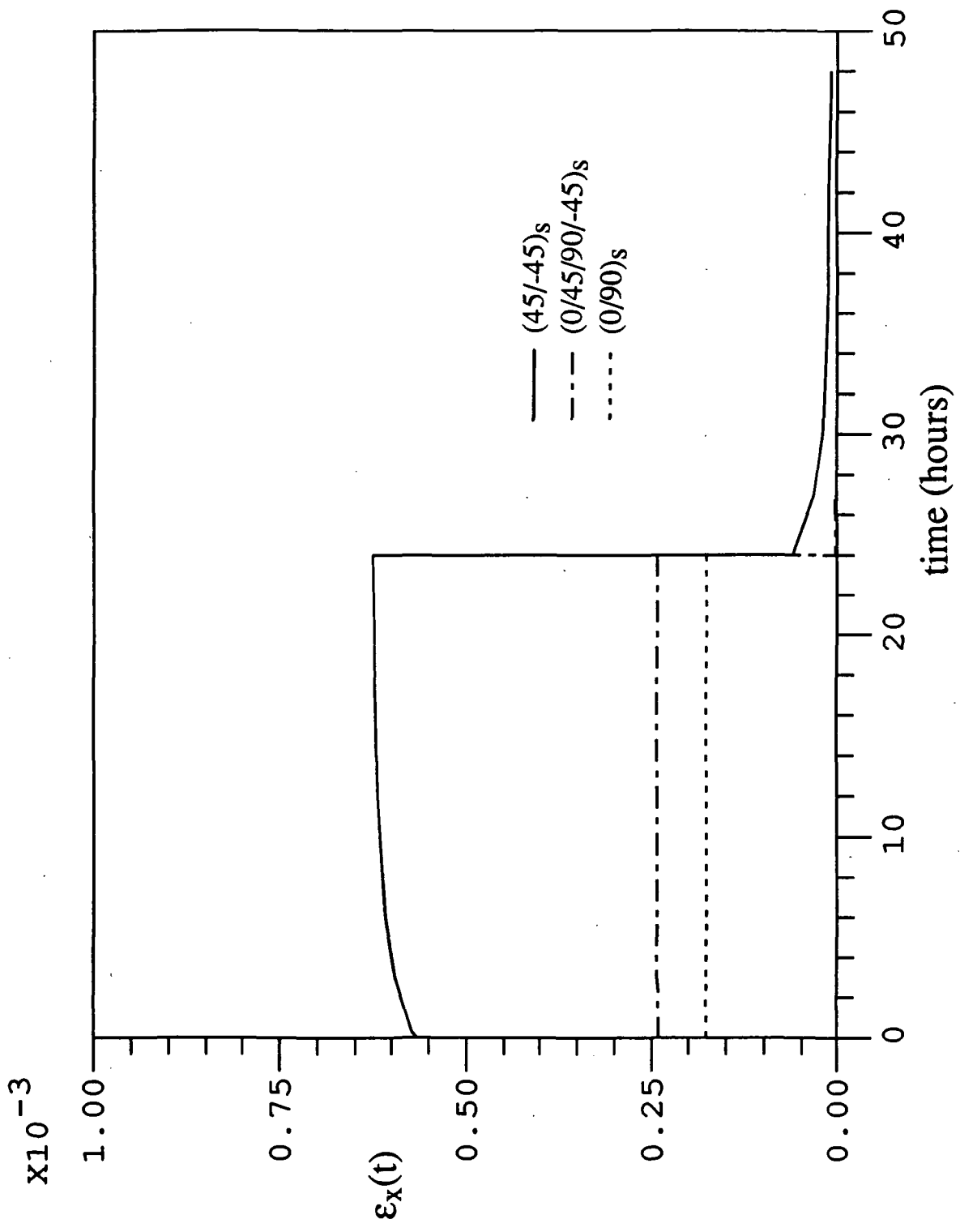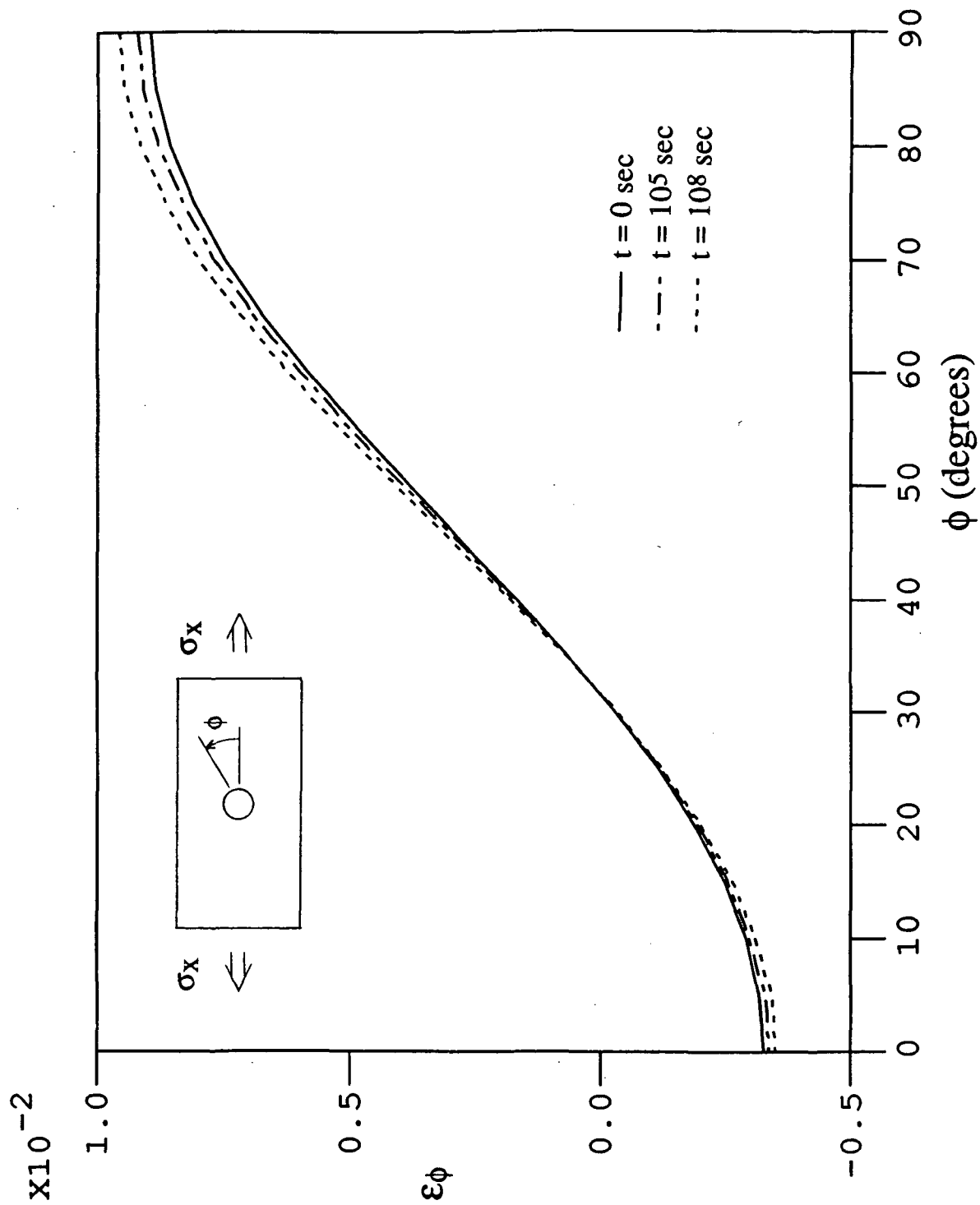
Fig. 13 Circumferential strains around a hole in a (0/45/90/-45)s laminate
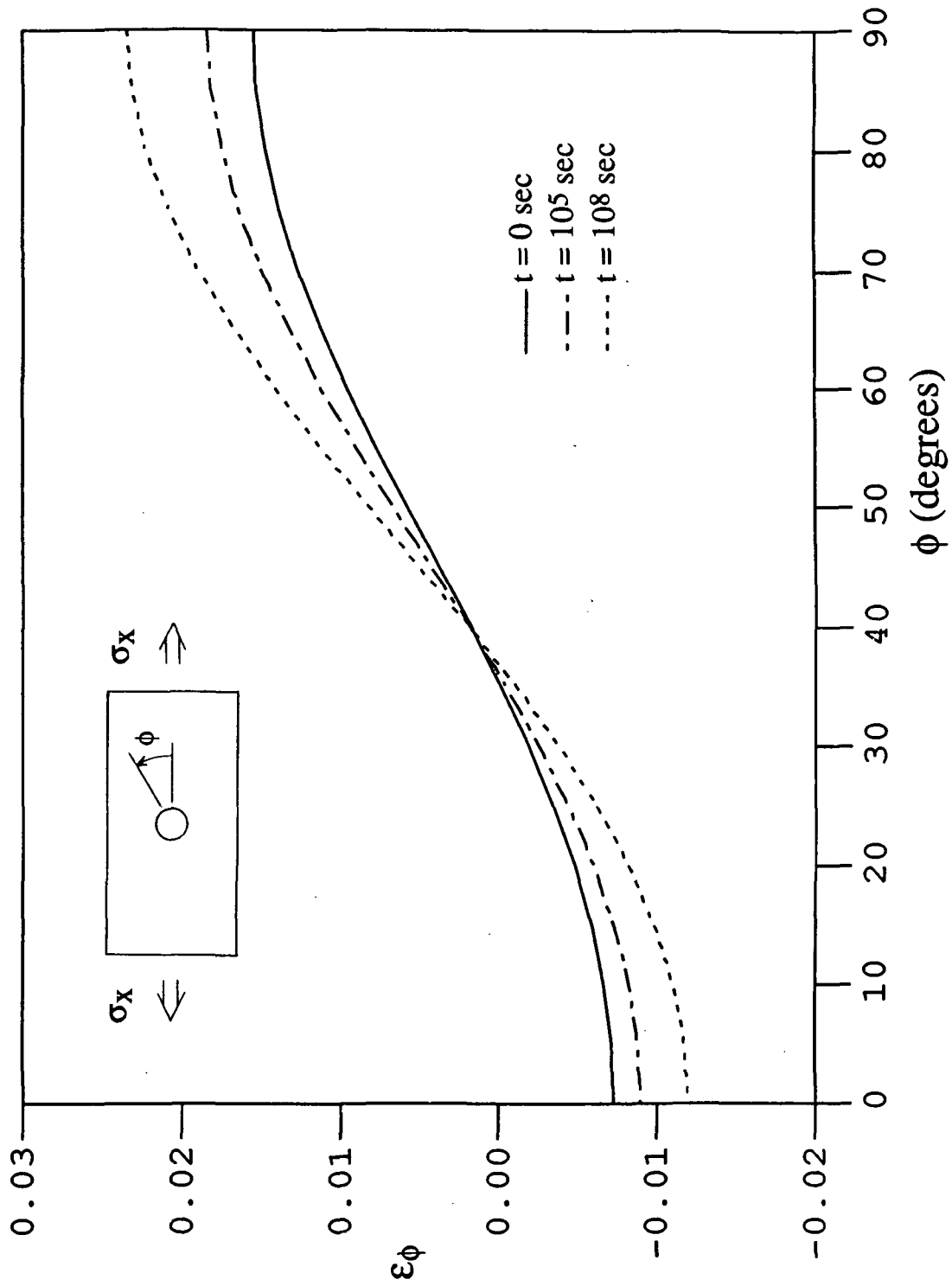
Fig. 14 Circumferential strains around a hole in a (45/-45)s laminate
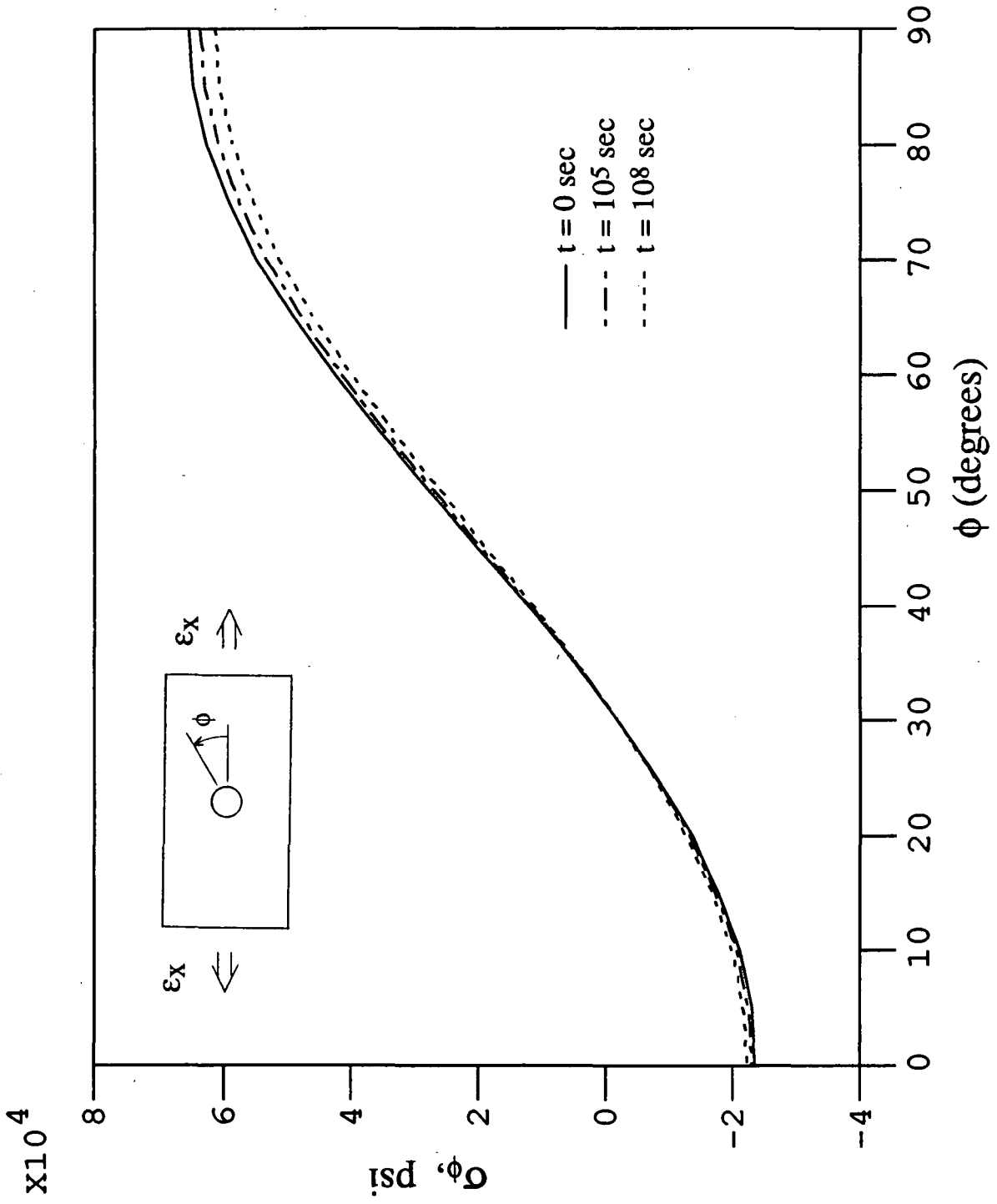
Fig. 15. Average circumferential stresses around a hole in $(0/45/90/-45)s$ laminate
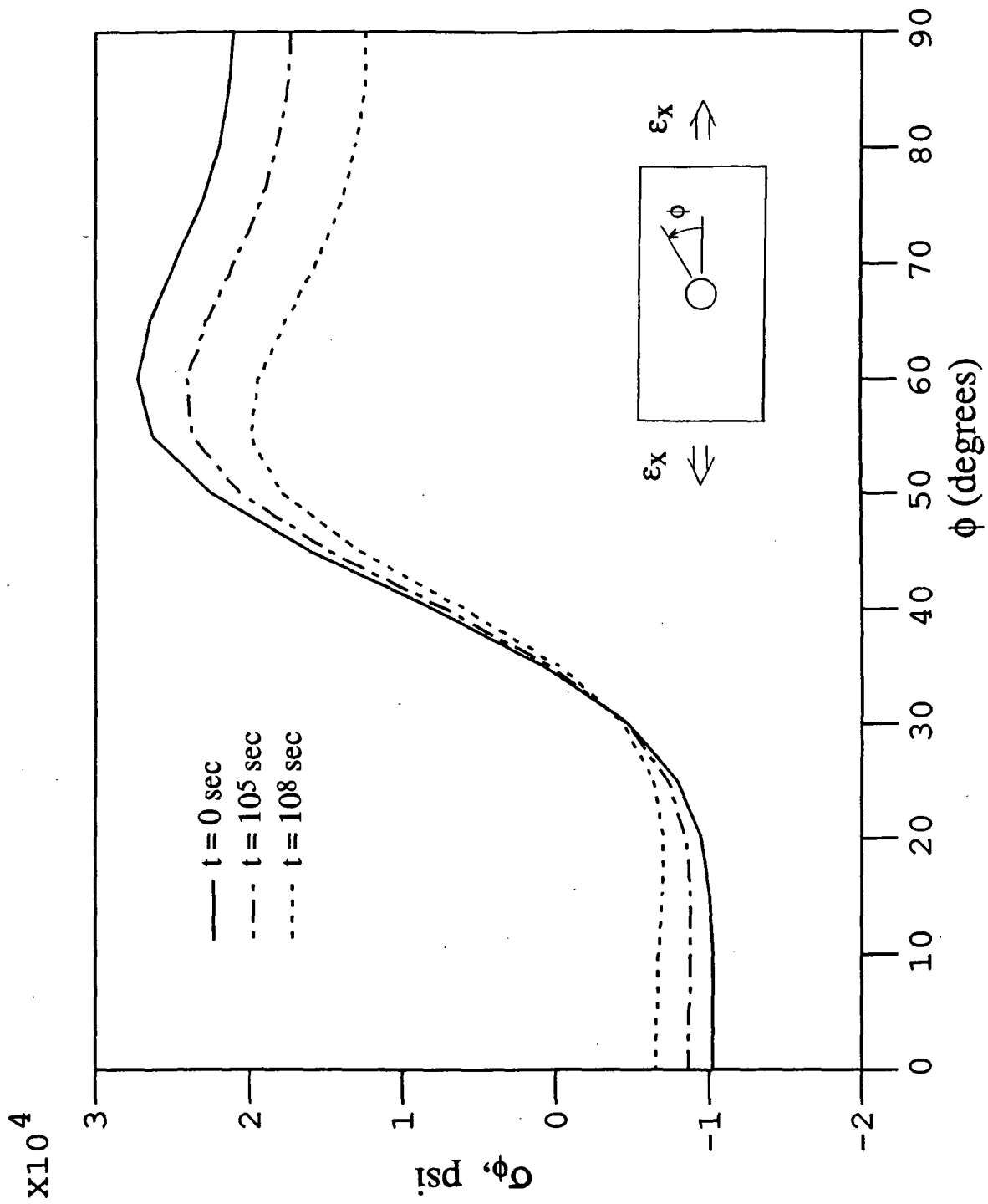
Fig. 16 Average circumferential stresses around a hole in $(45/-45)_s$ laminate
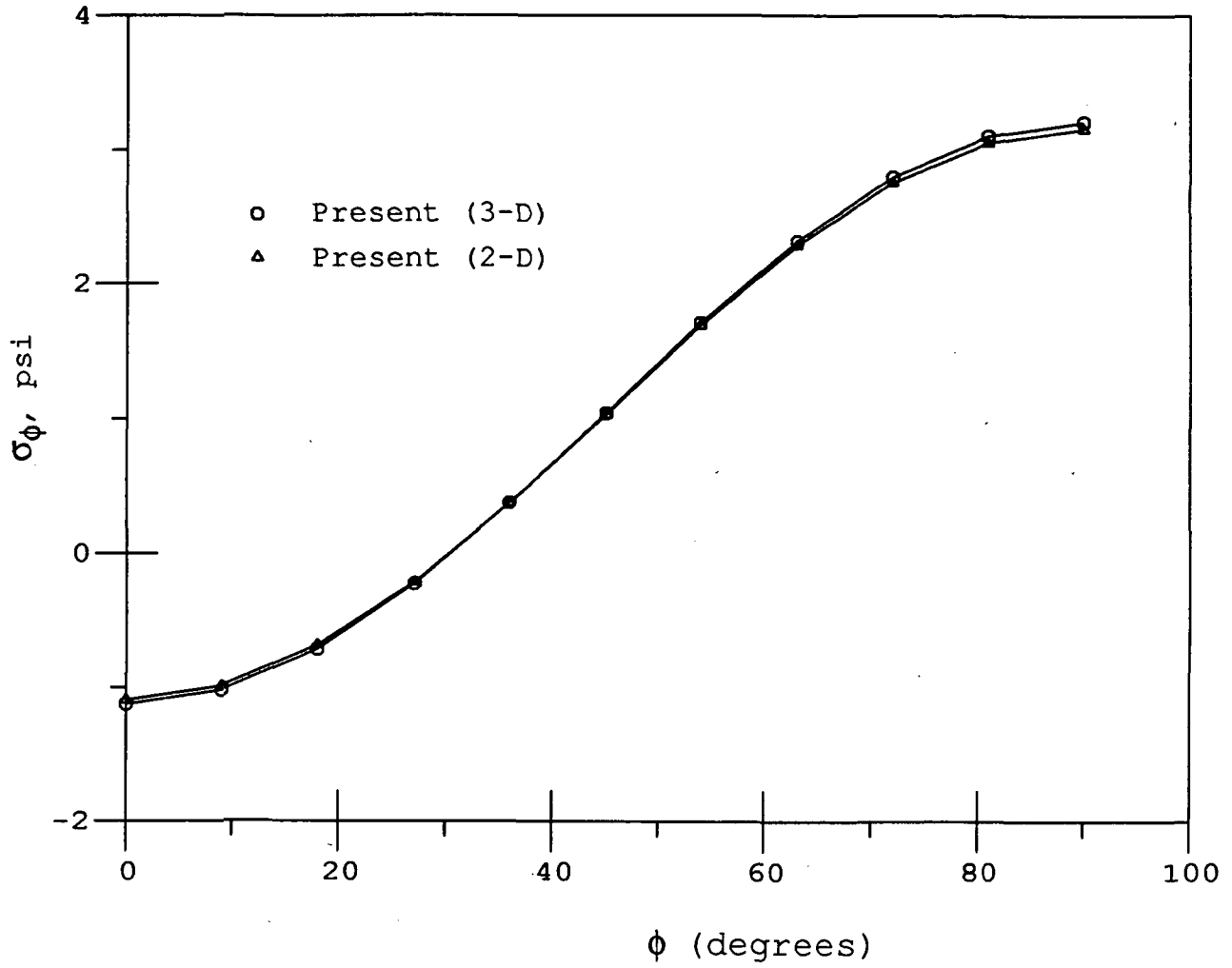
Fig. 17 Comparison of the 3-D and 2-D solutions
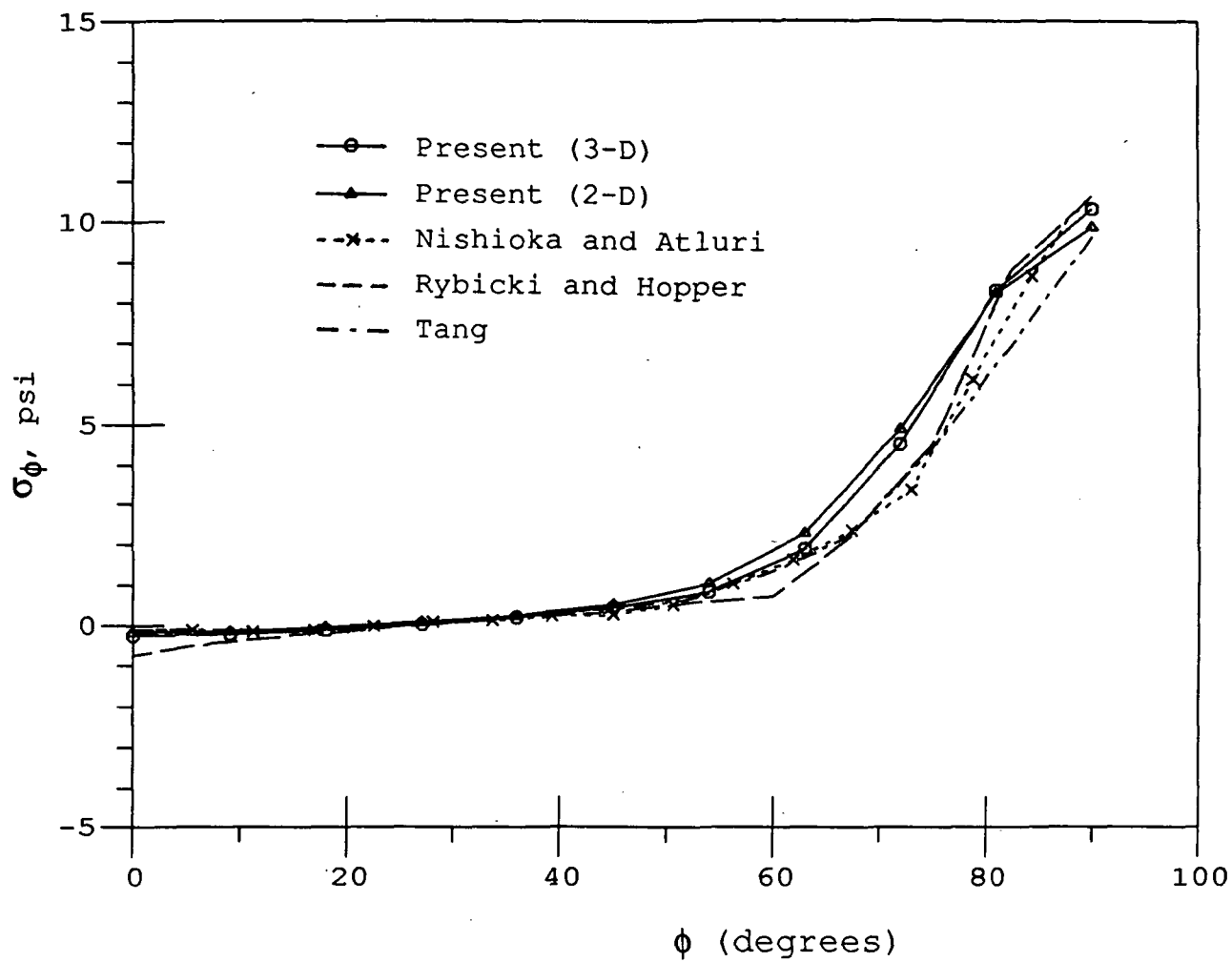
Fig. 18 Elastic σ_ϕ stresses in the 0° layer of a $(90/0)_s$ boron/epoxy laminate
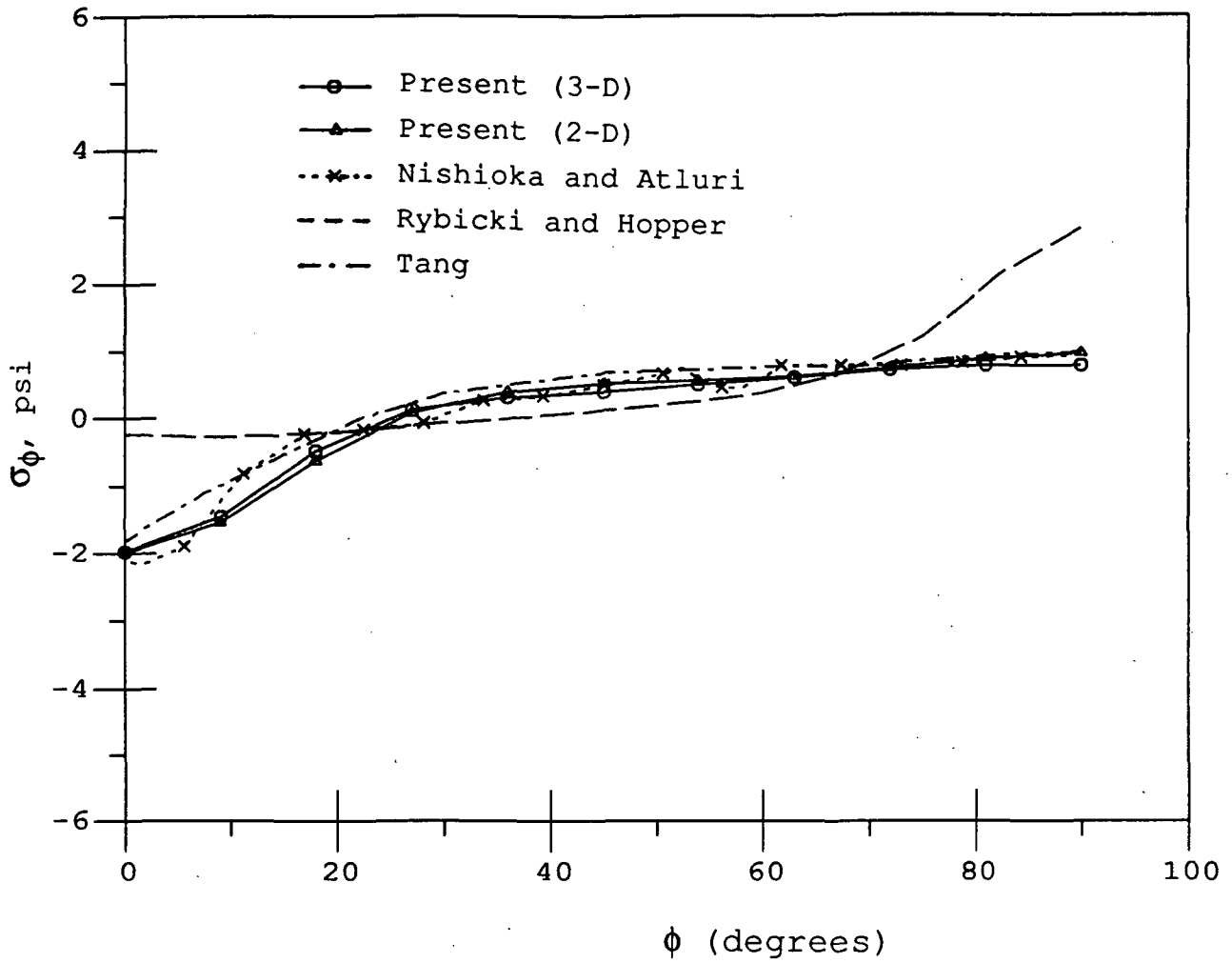
Fig. 19 Elastic σ_ϕ stresses in the 90° layer of a $(90/0)_S$ boron/epoxy laminate
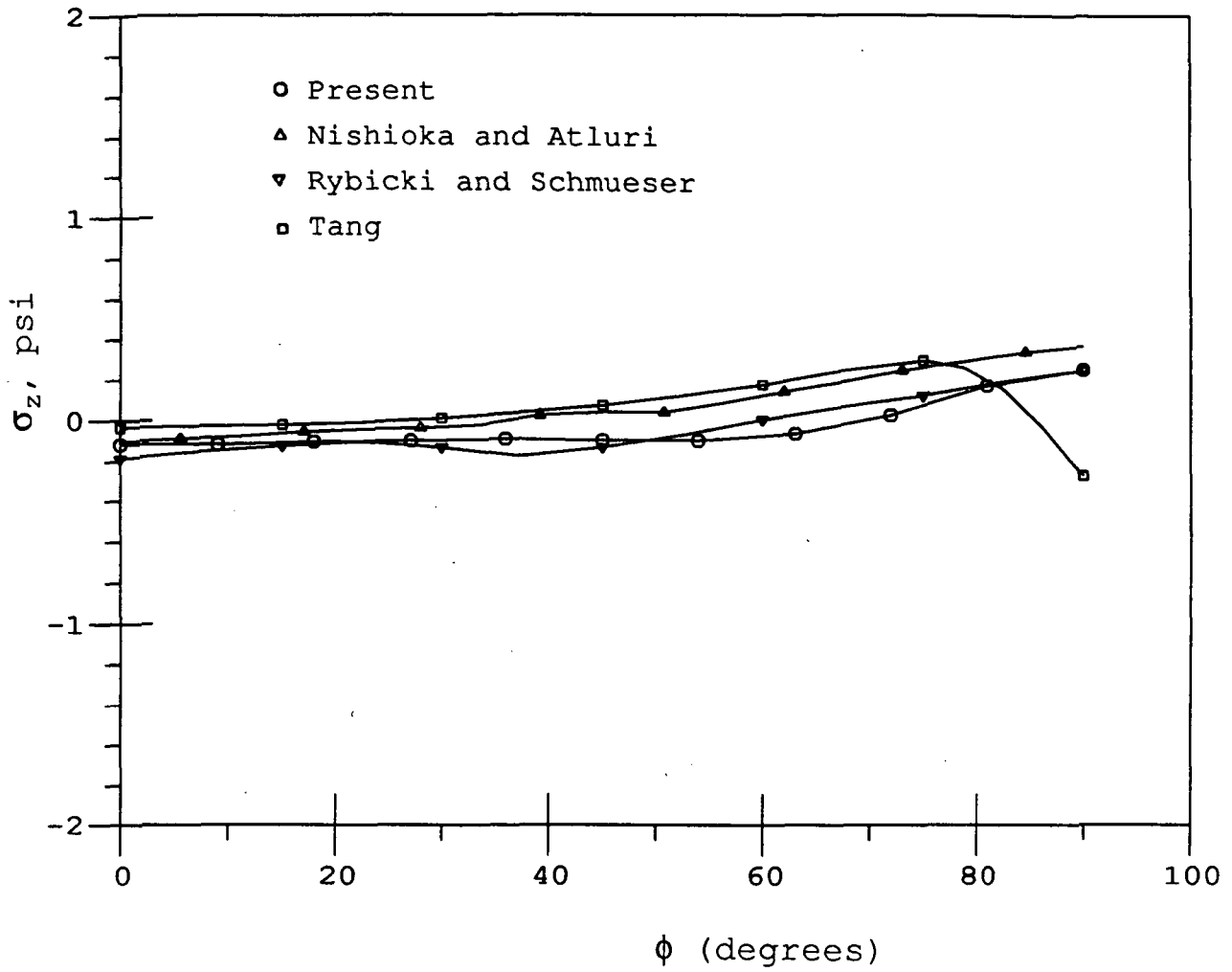
Fig. 20 Comparison of σ_Z stresses obtained from various solutions

L = 1.0"
W = 0.5"
a = 0.125"
2h = 0.125"
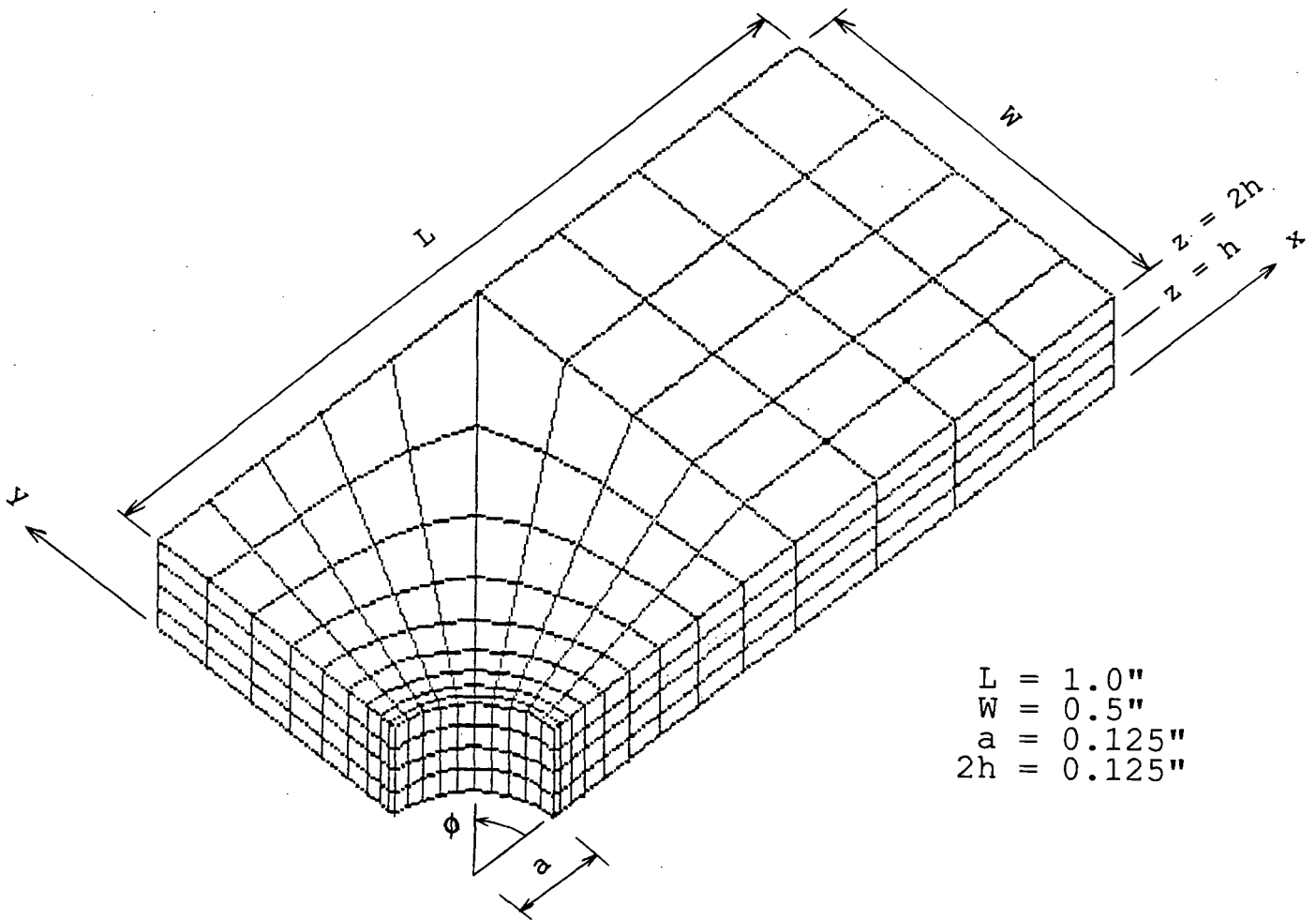
Fig. 21 Finite element mesh pattern used for cross-ply laminates
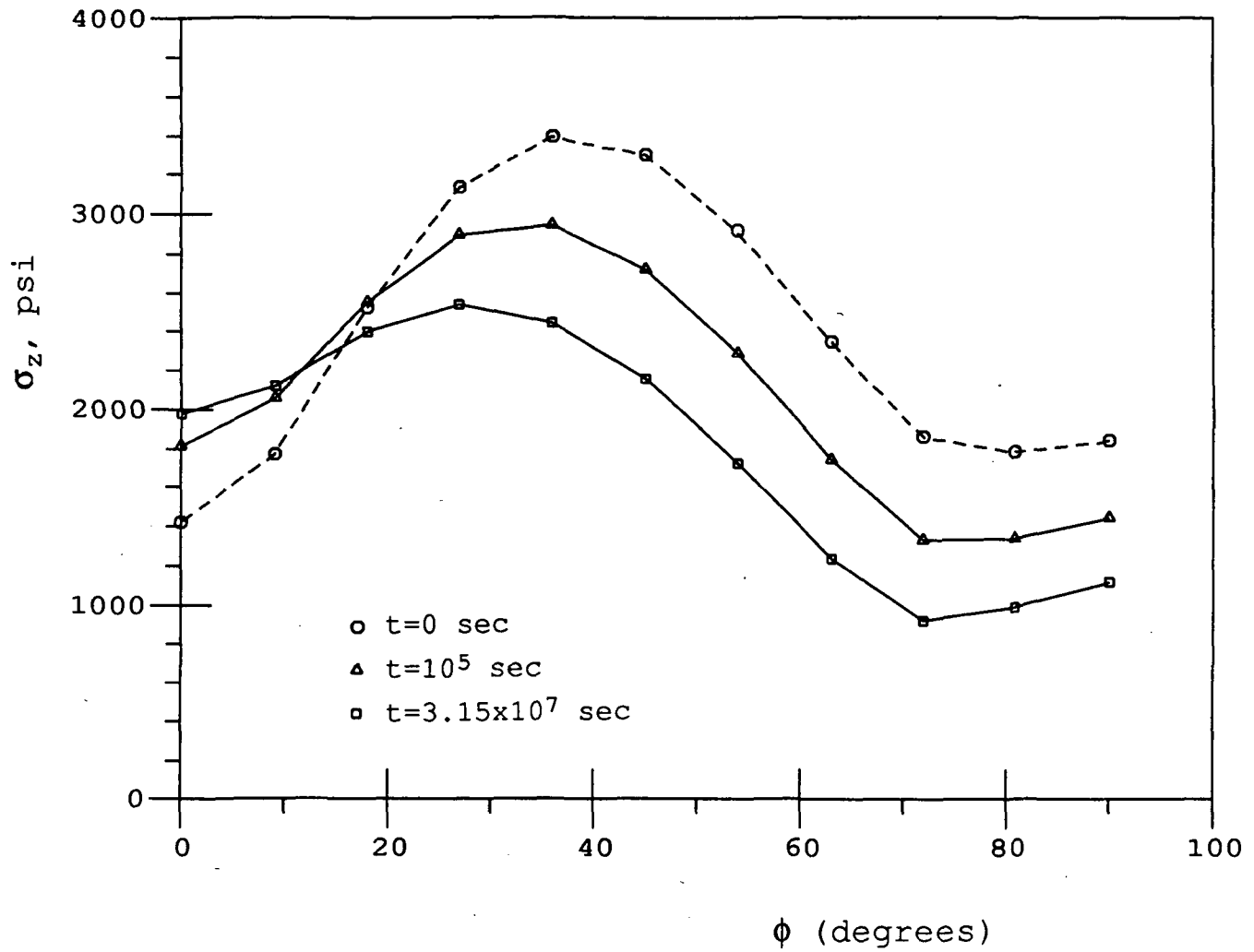
Fig. 22 Interlaminar normal stress σ_z at the mid-plane in a $(0/90)_s$ laminate
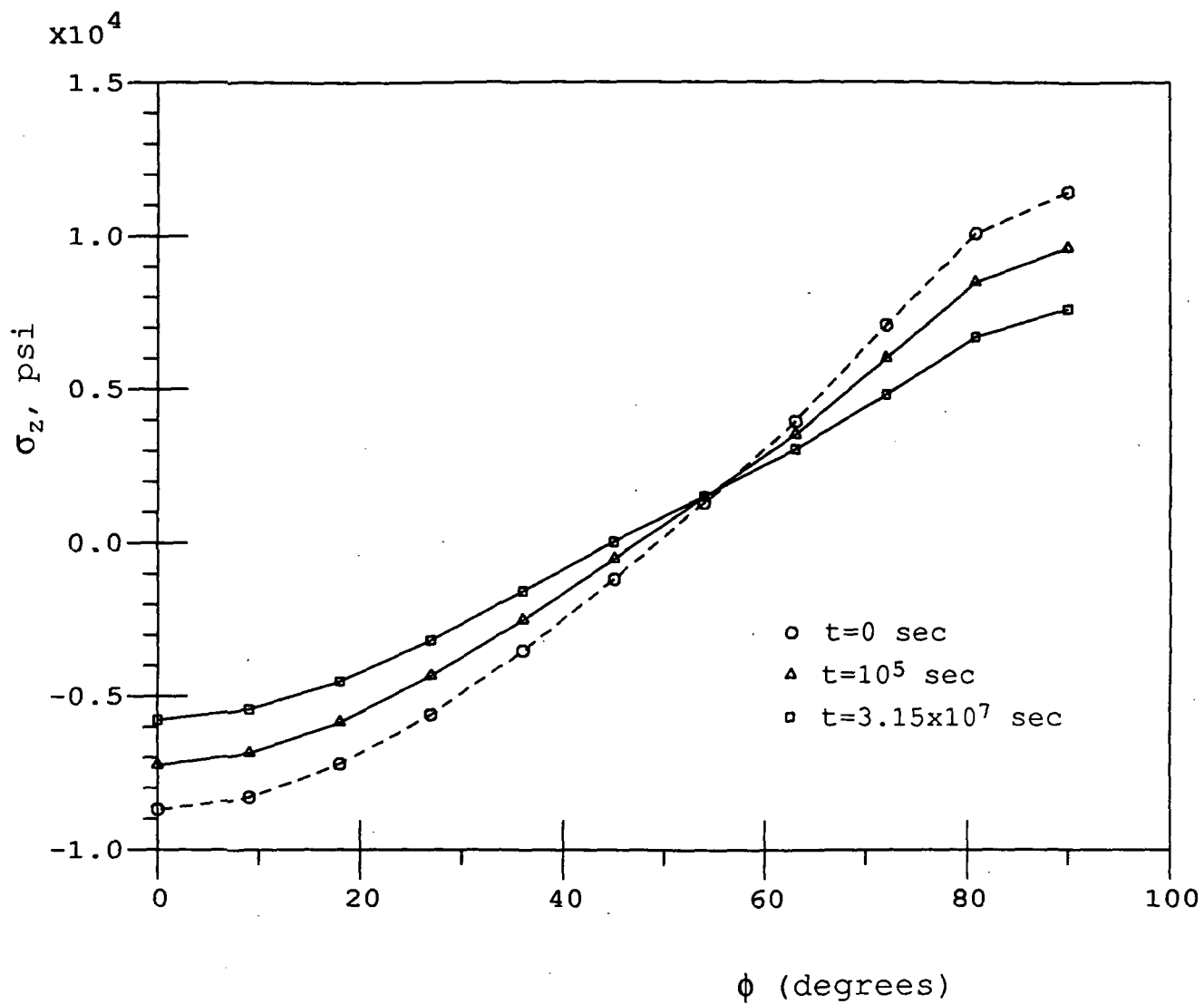
Fig. 23 Interlaminar normal stress σ_z at the mid-plane in a $(90/0)_s$ laminate
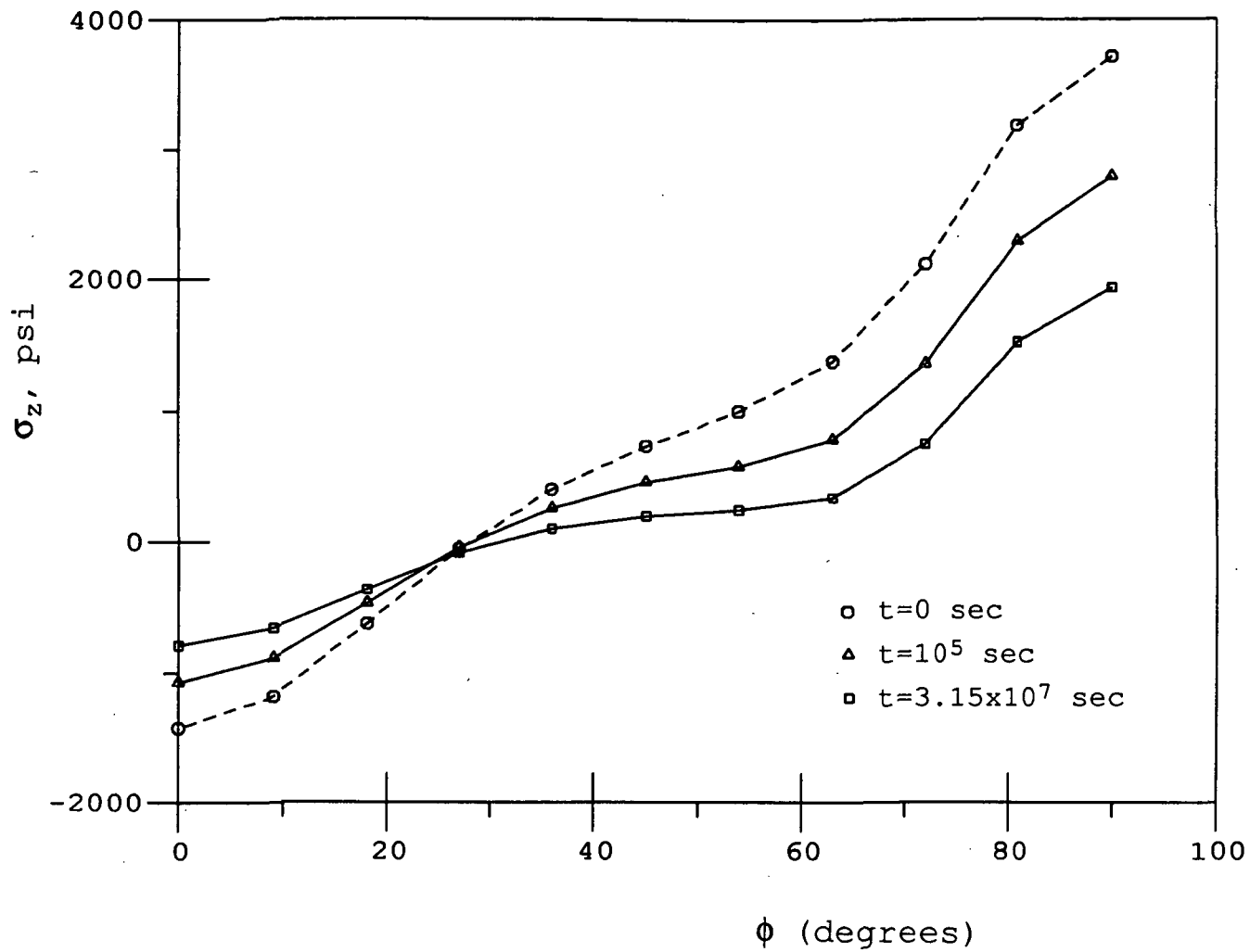
Fig. 24 Interlaminar normal stress σ_z at the interface in a $(0/90)_s$ laminate
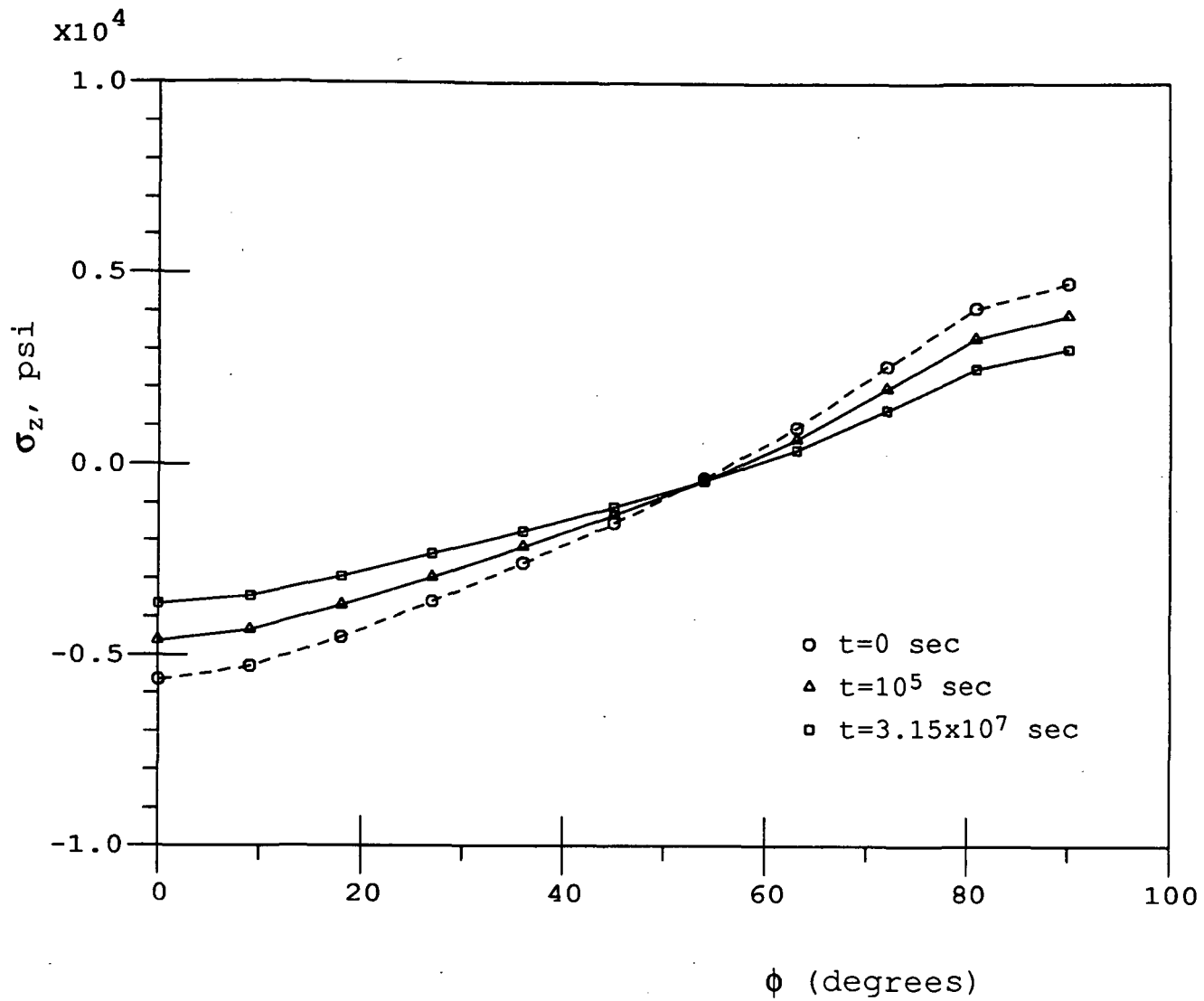
Fig. 25 Interlaminar normal stress σ_z at the interface in a $(90/0)_s$ laminate
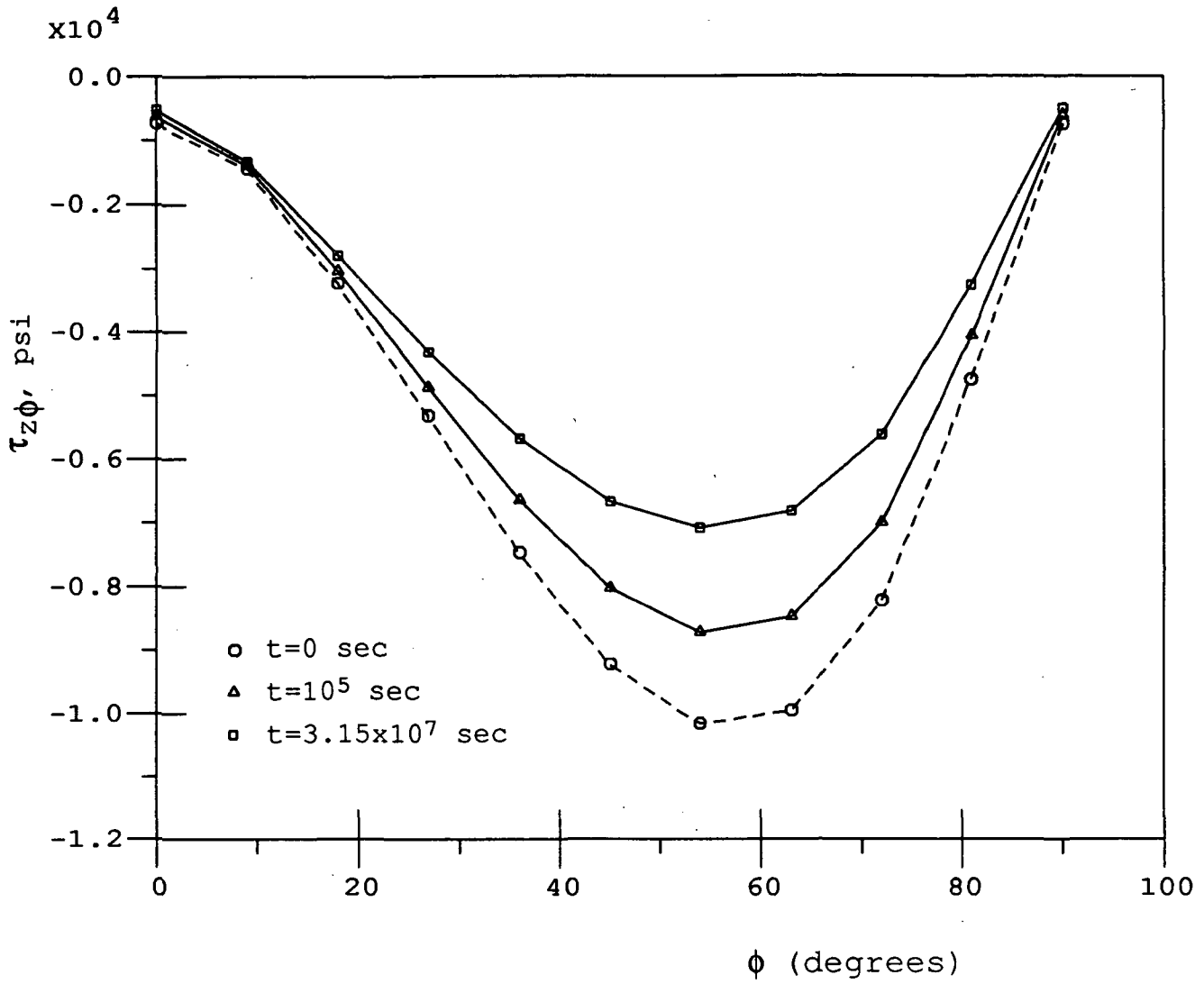
Fig. 26 Interlaminar shear stress $\tau_{z\phi}$ at the interface in a $(0/90)_s$ laminate
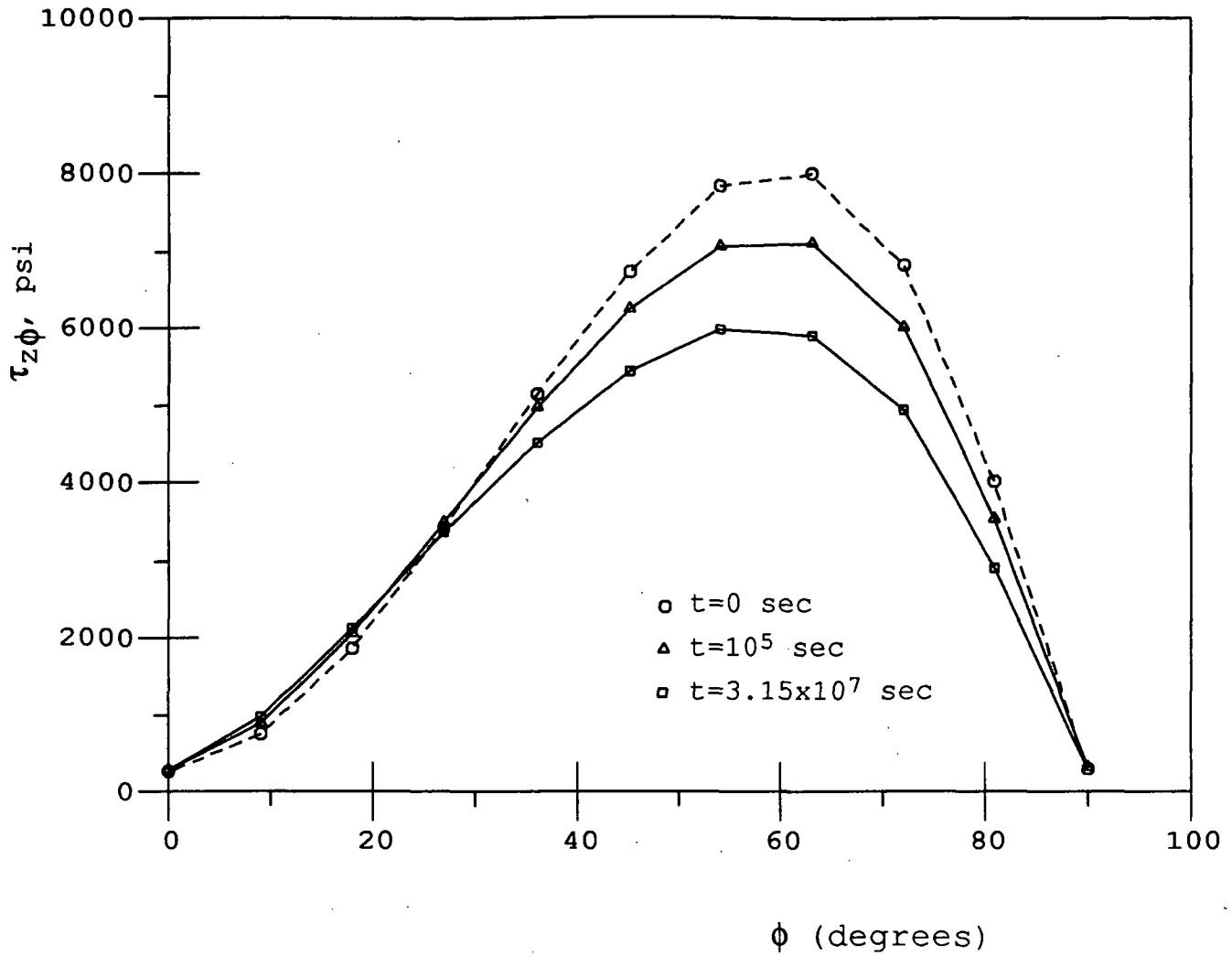
Fig. 27 Interlaminar shear stress $\tau_{z\phi}$ at the interface in a $(90/0)_s$ laminate
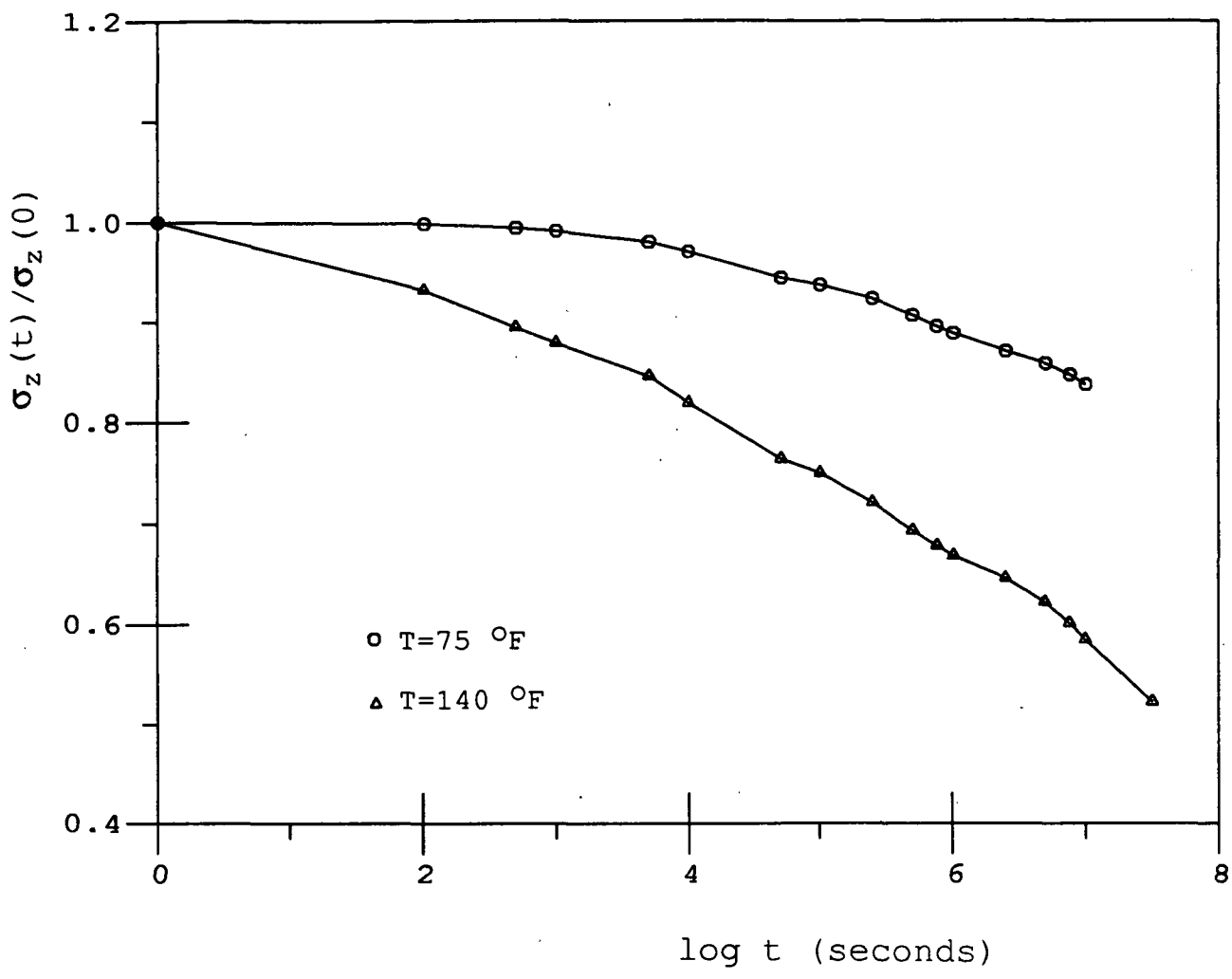
Fig. 28 History of the interlaminar normal stress at the interface of a (0/90)$_S$ laminate
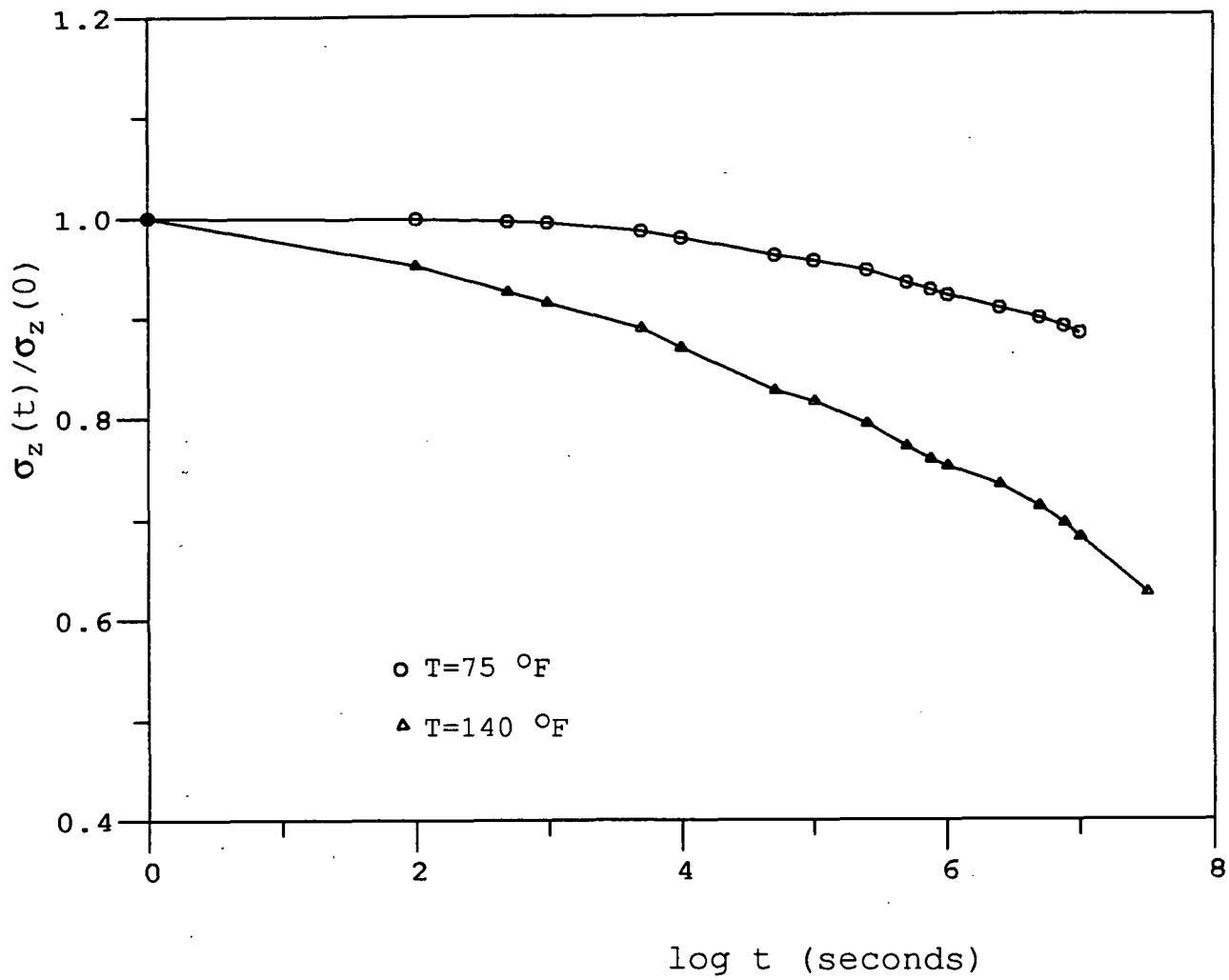
Fig. 29 History of the interlaminar normal stress at the interface of a (90/0)$_S$ laminate
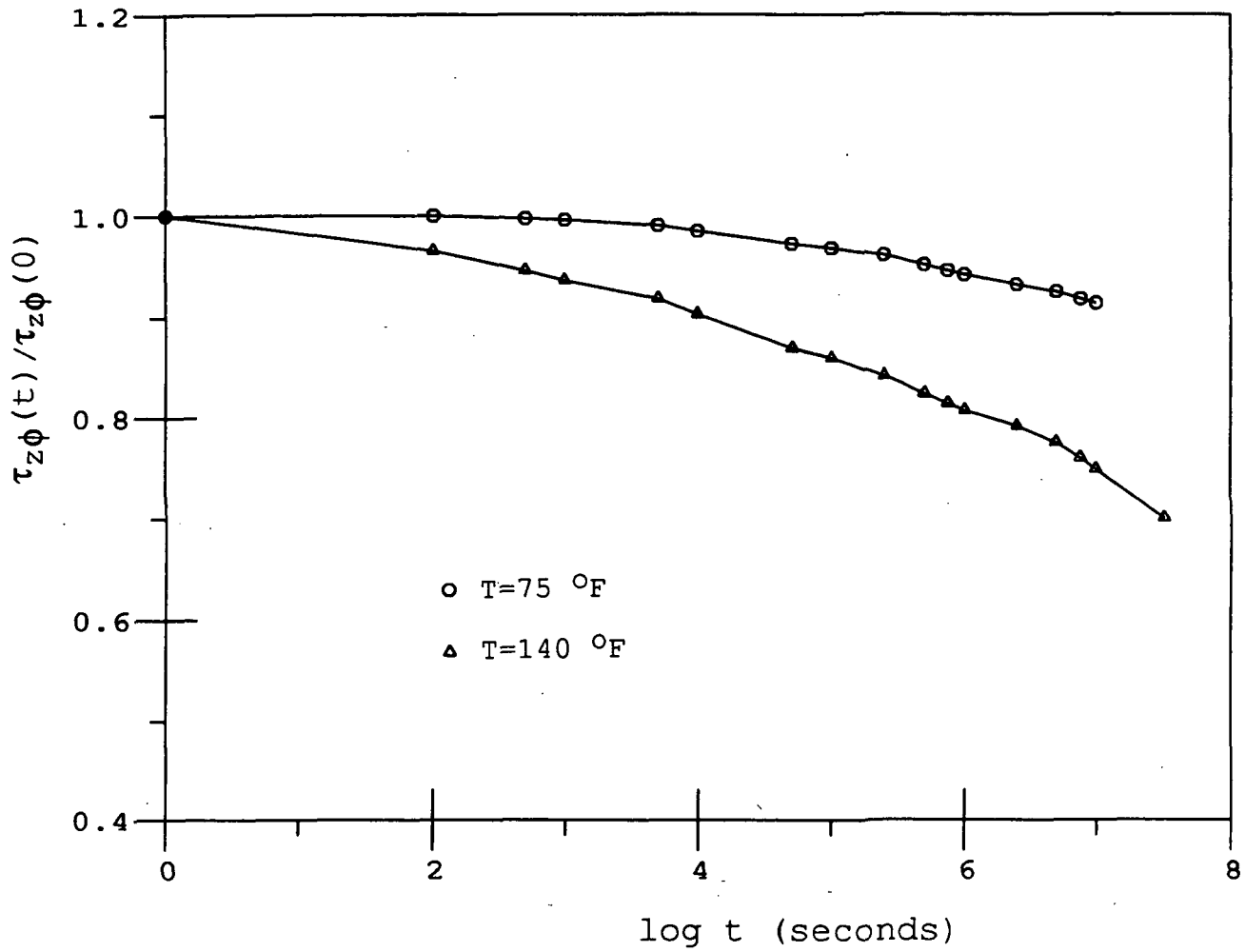
Fig. 30 History of the interlaminar shear stress at the interface of a (0/90)s laminate

L = 1.0"
W = 0.5"
a = 0.125"
2h = 0.125"
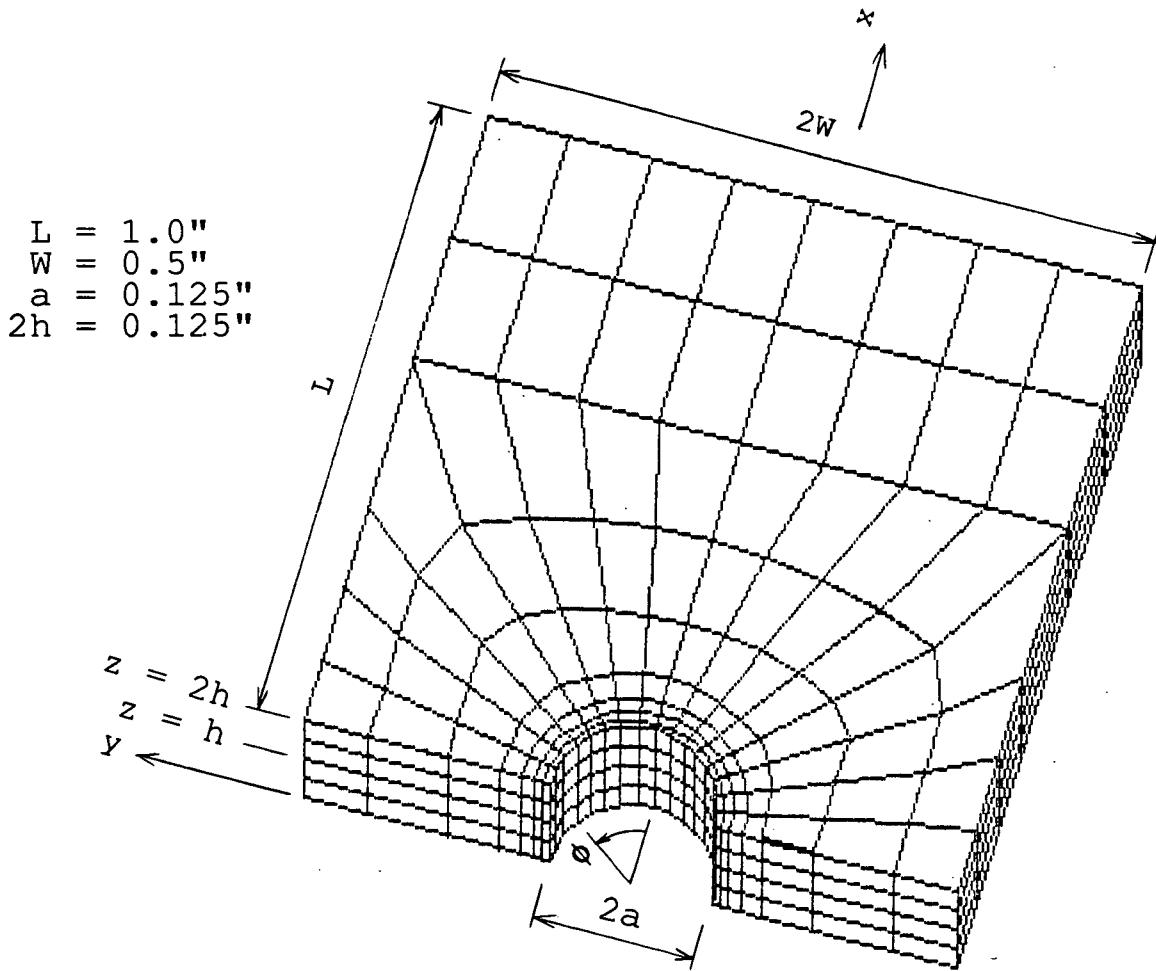
Fig. 31 Finite element mesh pattern for a (45/-45)s laminate
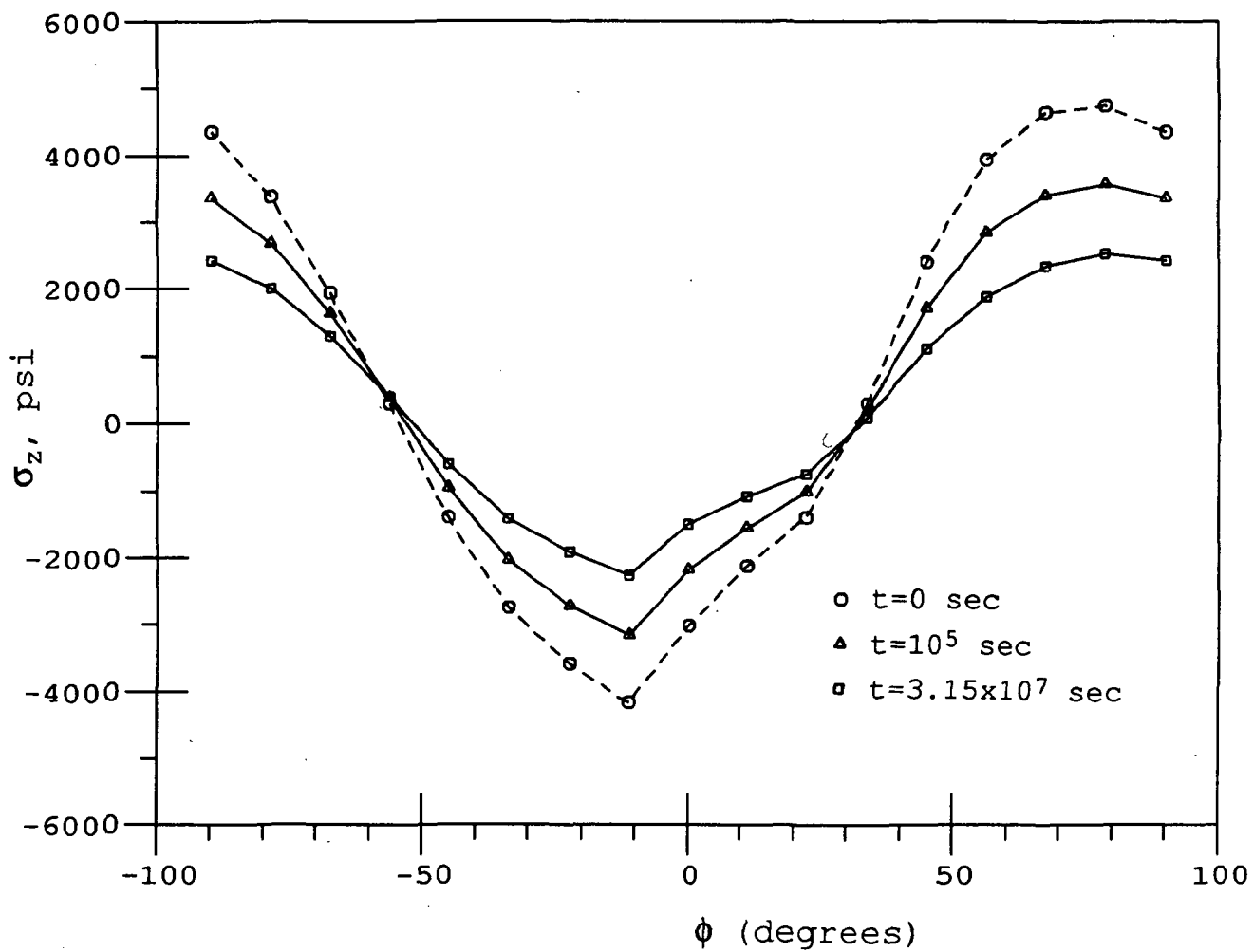
Fig. 32 Interlaminar normal stress σ_z at the mid-plane in a $(45/-45)_S$ laminate
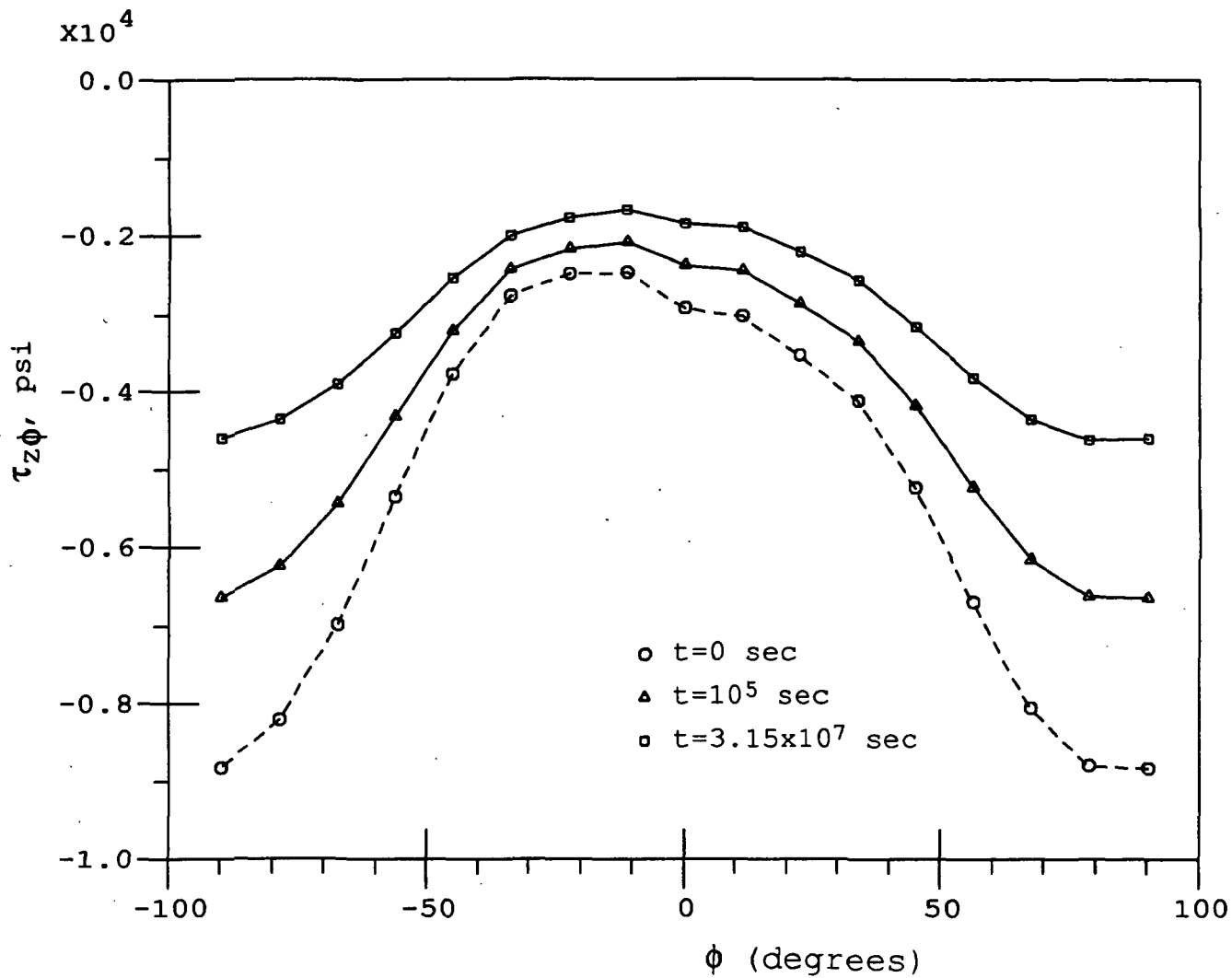
Fig. 33 Interlaminar shear stress $\tau_{z\phi}$ at the interface in a $(45/-45)_S$ laminate
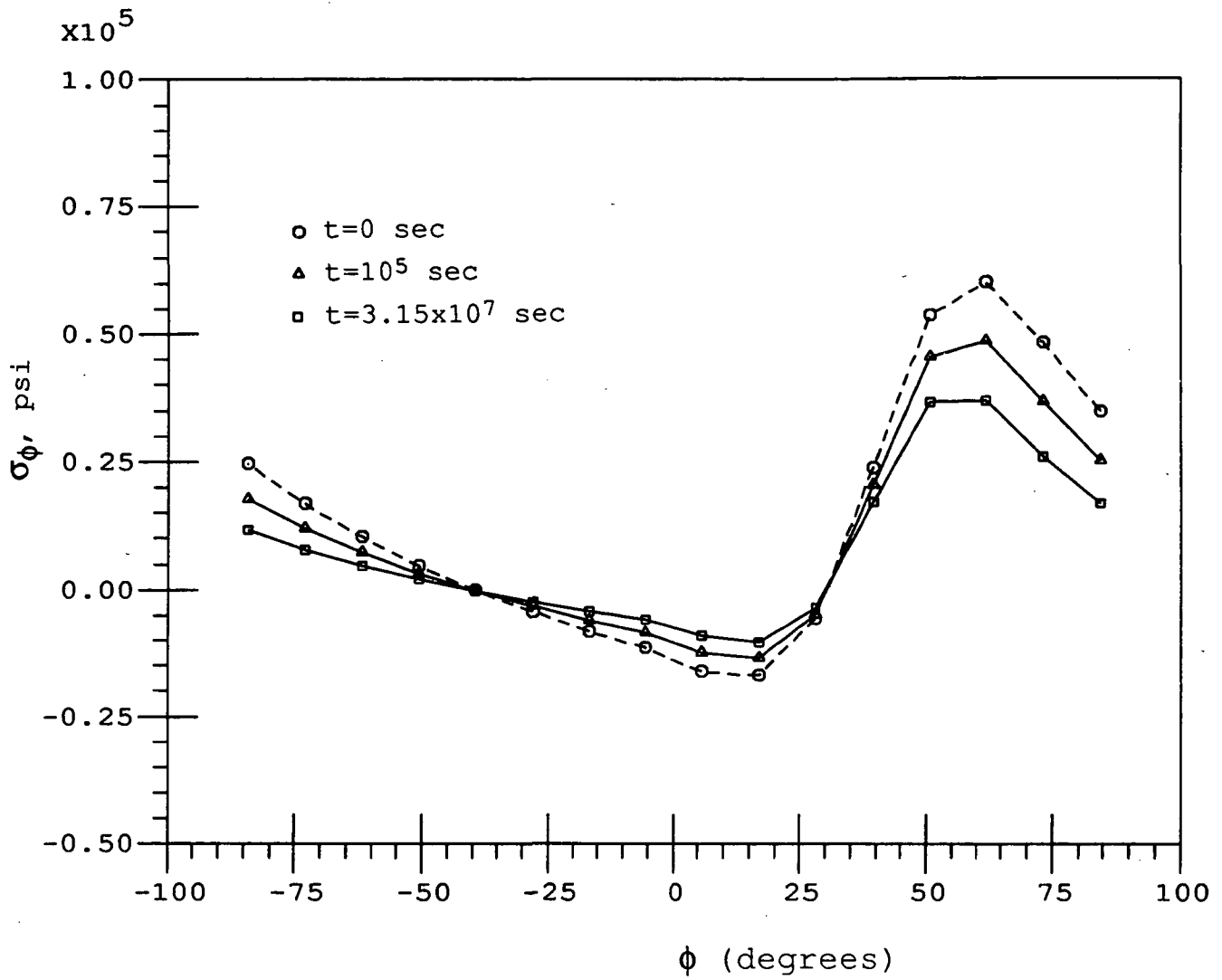
Fig. 34 Circumferential stress σ_ϕ in the -45° ply of the (45/-45)$_s$ laminate
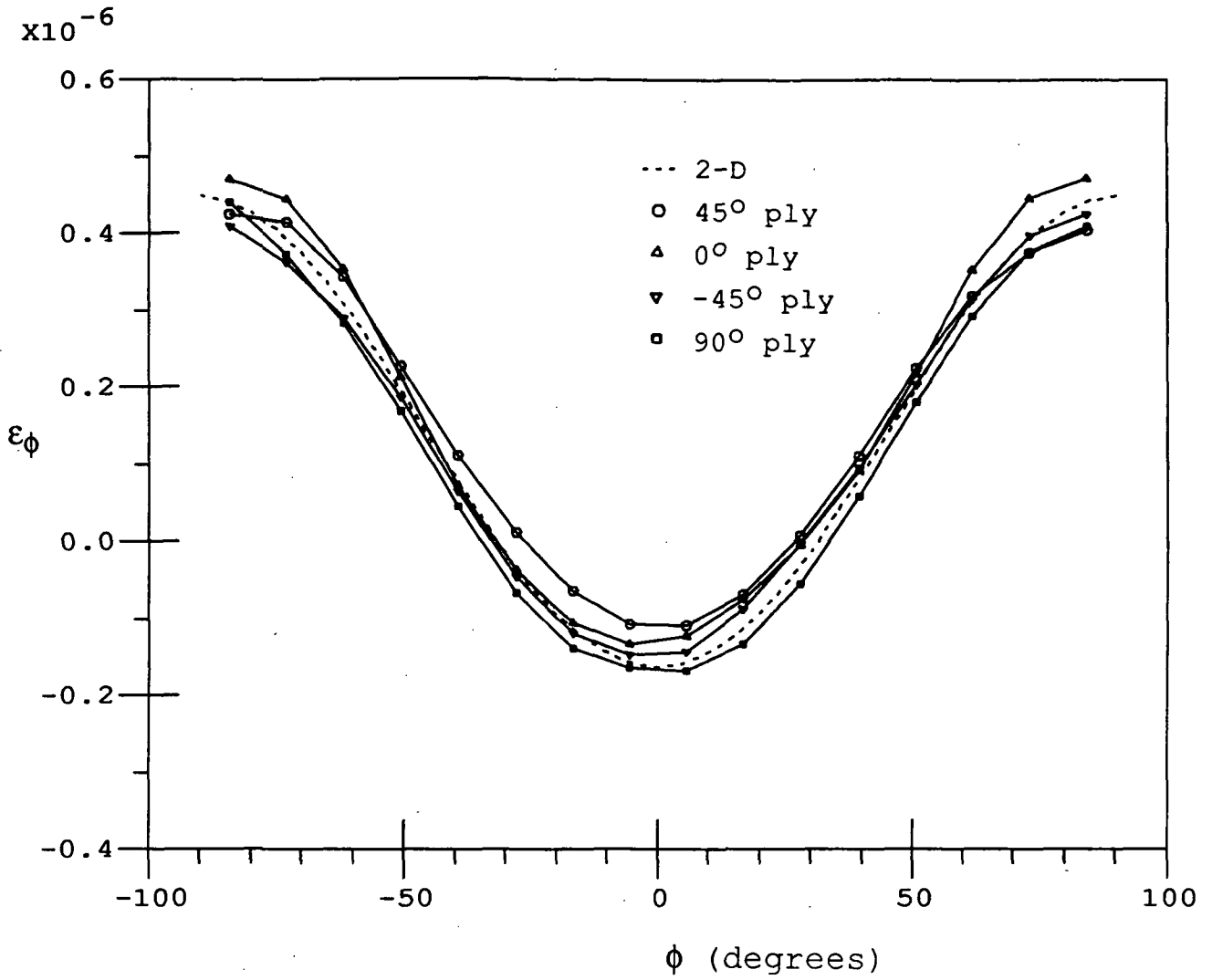
Fig. 35 Comparison of elastic ply strains ε_ϕ with the 2-D solution for a $(45/0/-45/90)_S$ laminate
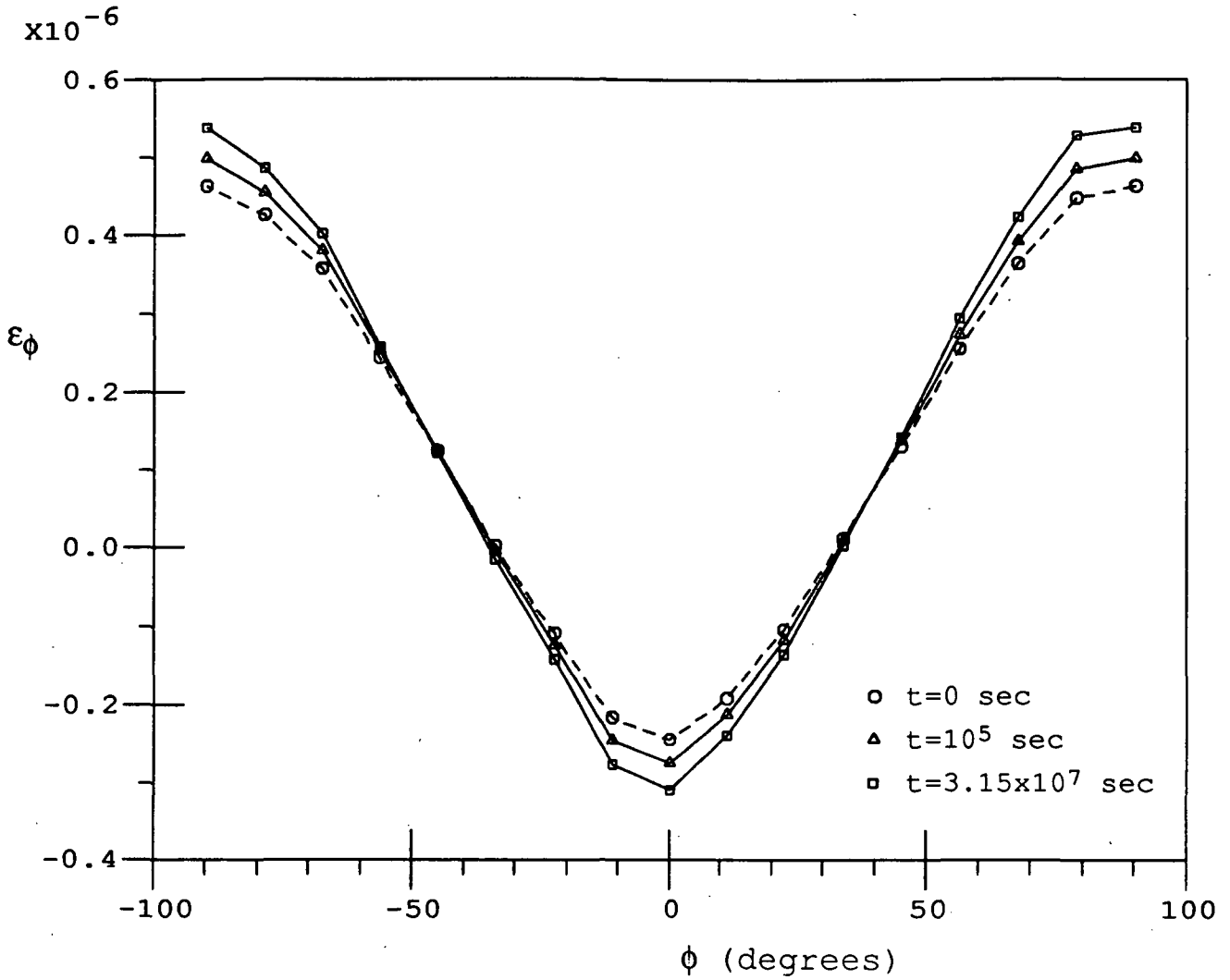
Fig. 36 Circumferential strain ε_ϕ in the 90° ply of a (45/0/-45/90)$_S$ laminate
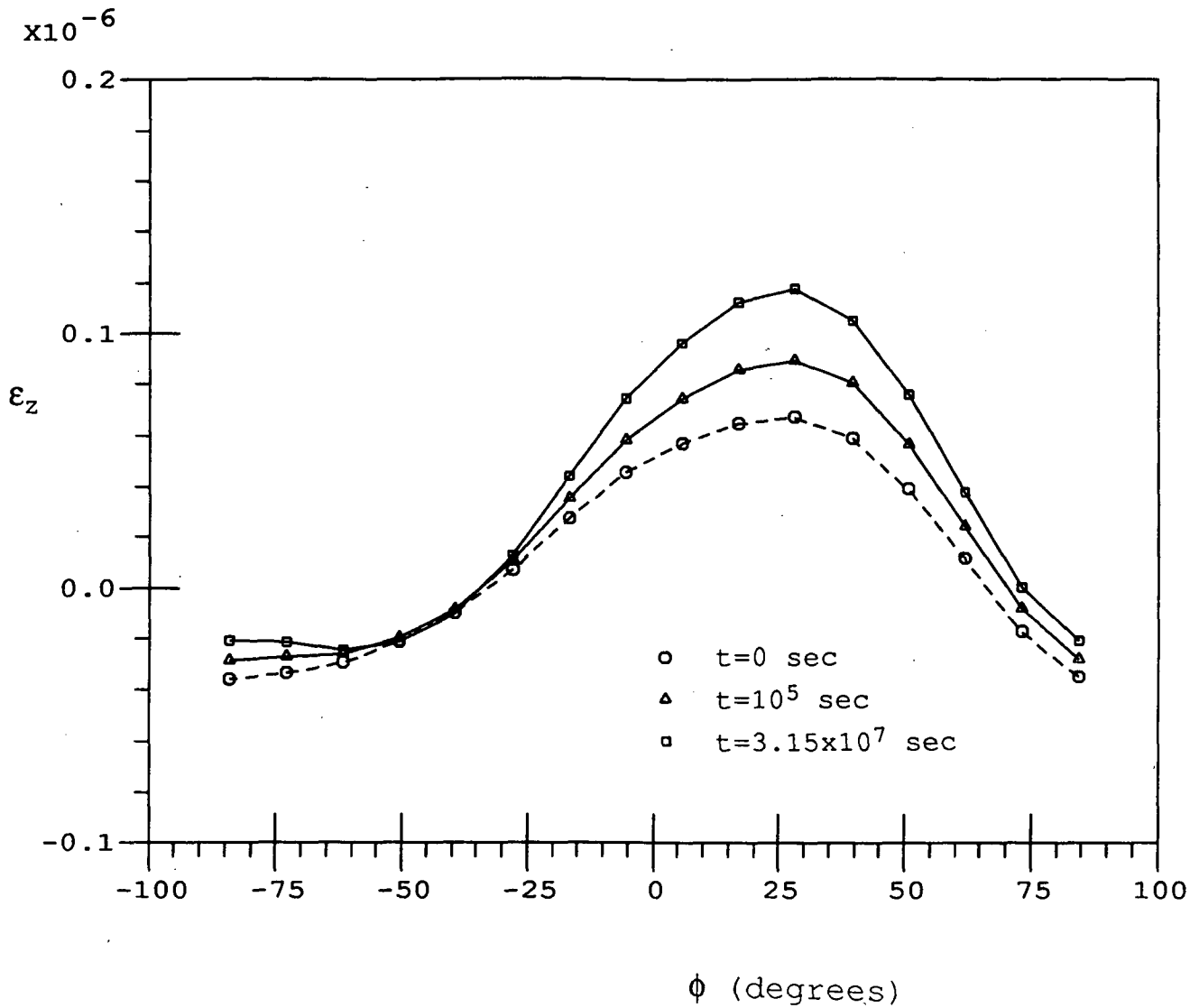
Fig. 37 Transverse strain ε_z in the 90° ply of a $(45/0/-45/90)_s$ laminate
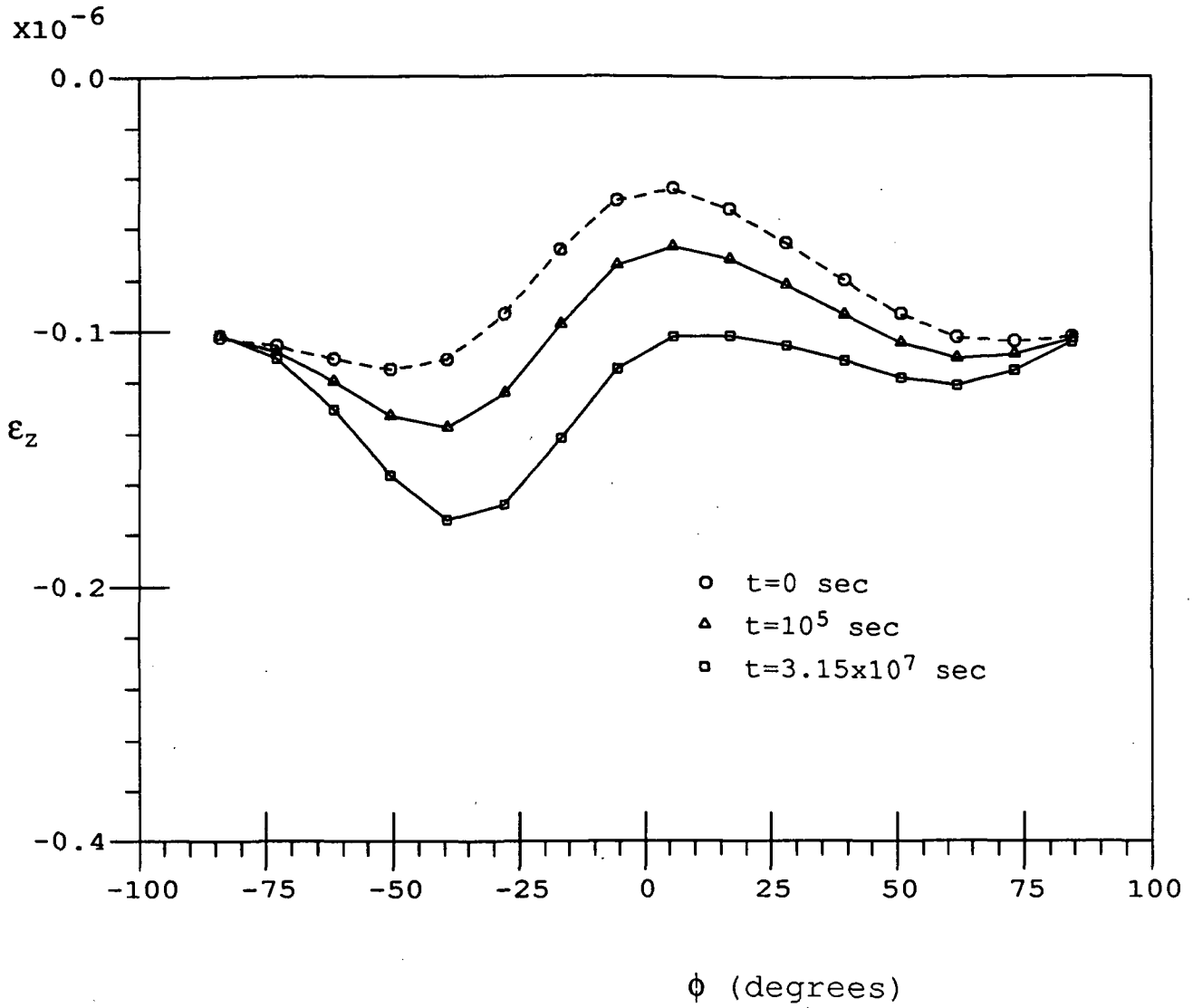
Fig. 38 Transverse strain ε_z in the 0° ply of a $(45/0/-45/90)_s$ laminate
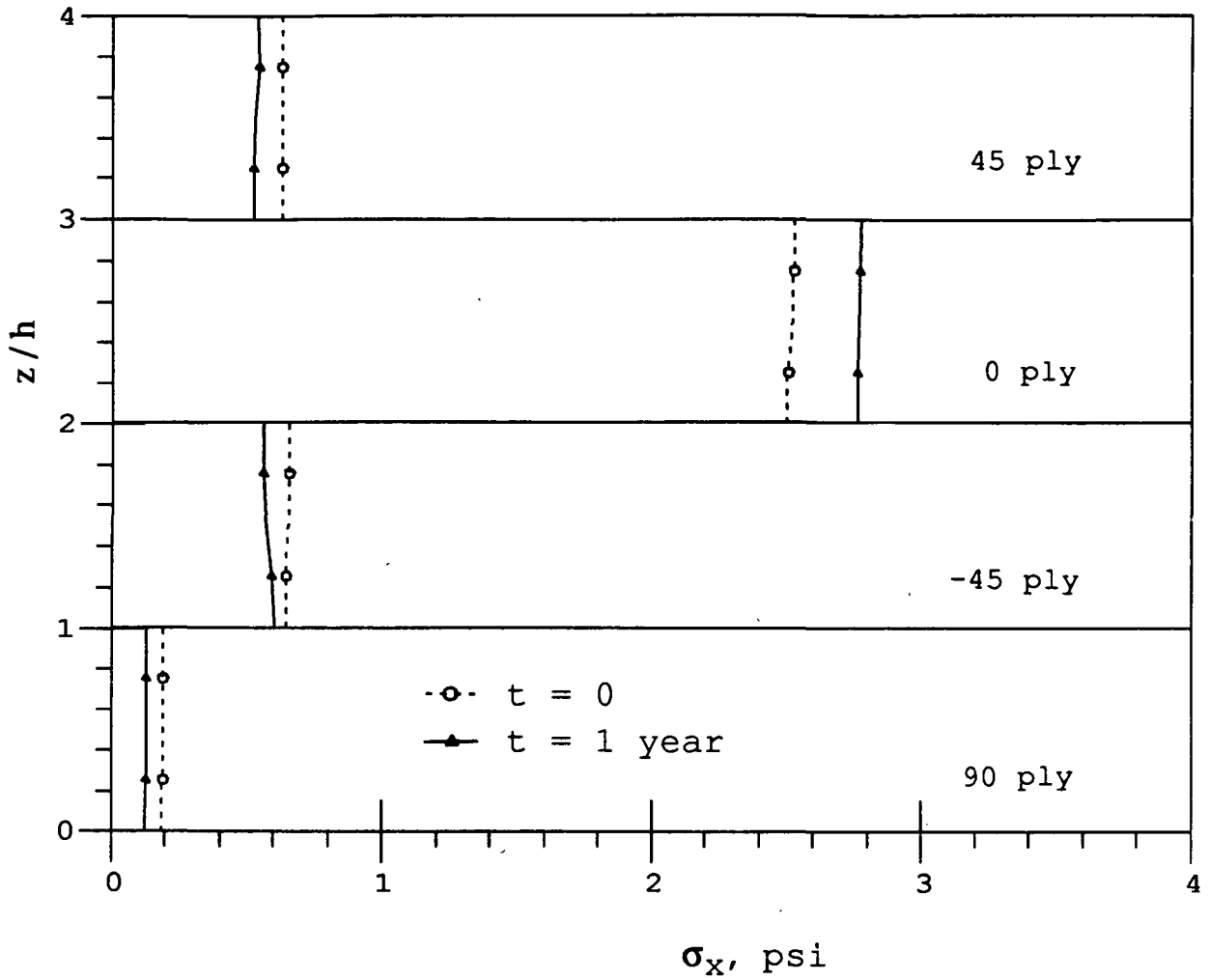
Fig. 39 Through-the-thickness stress distributions (x/L = 0.9, y/W = 0.125)
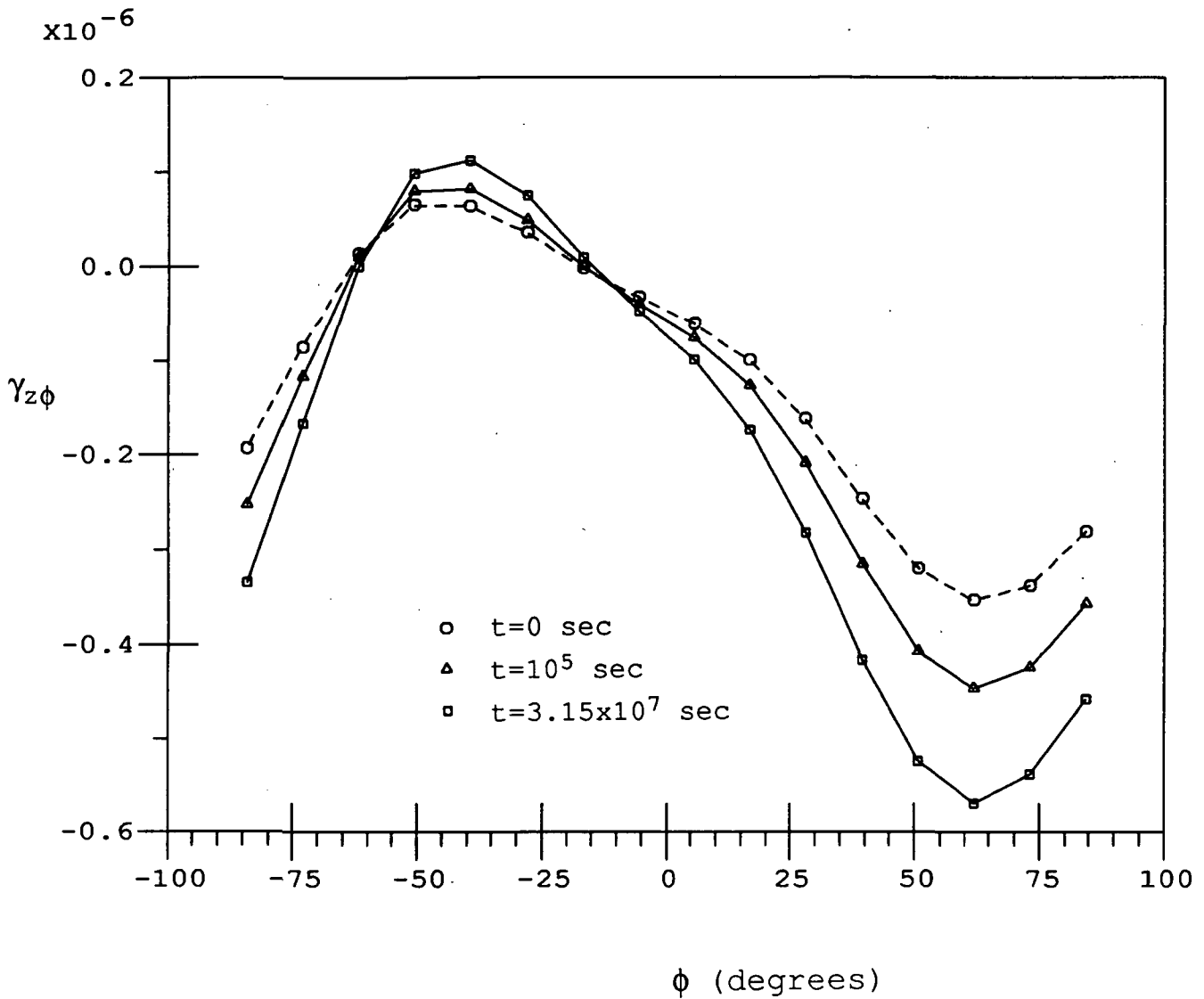
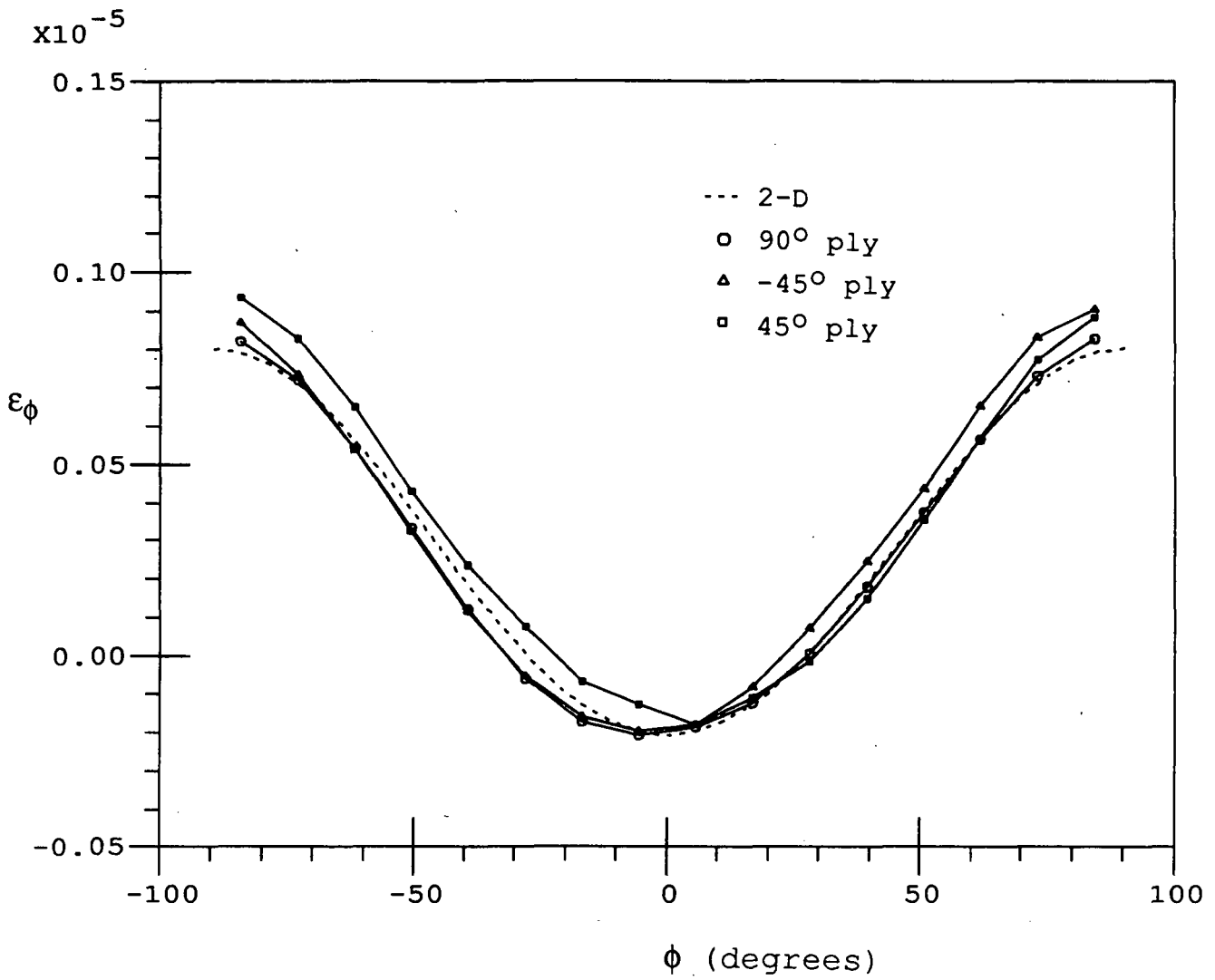Fig. 40 Transverse shear strain $\gamma_{z\phi}$ in the -45° ply of a $(45/0/-45/90)_s$ laminate

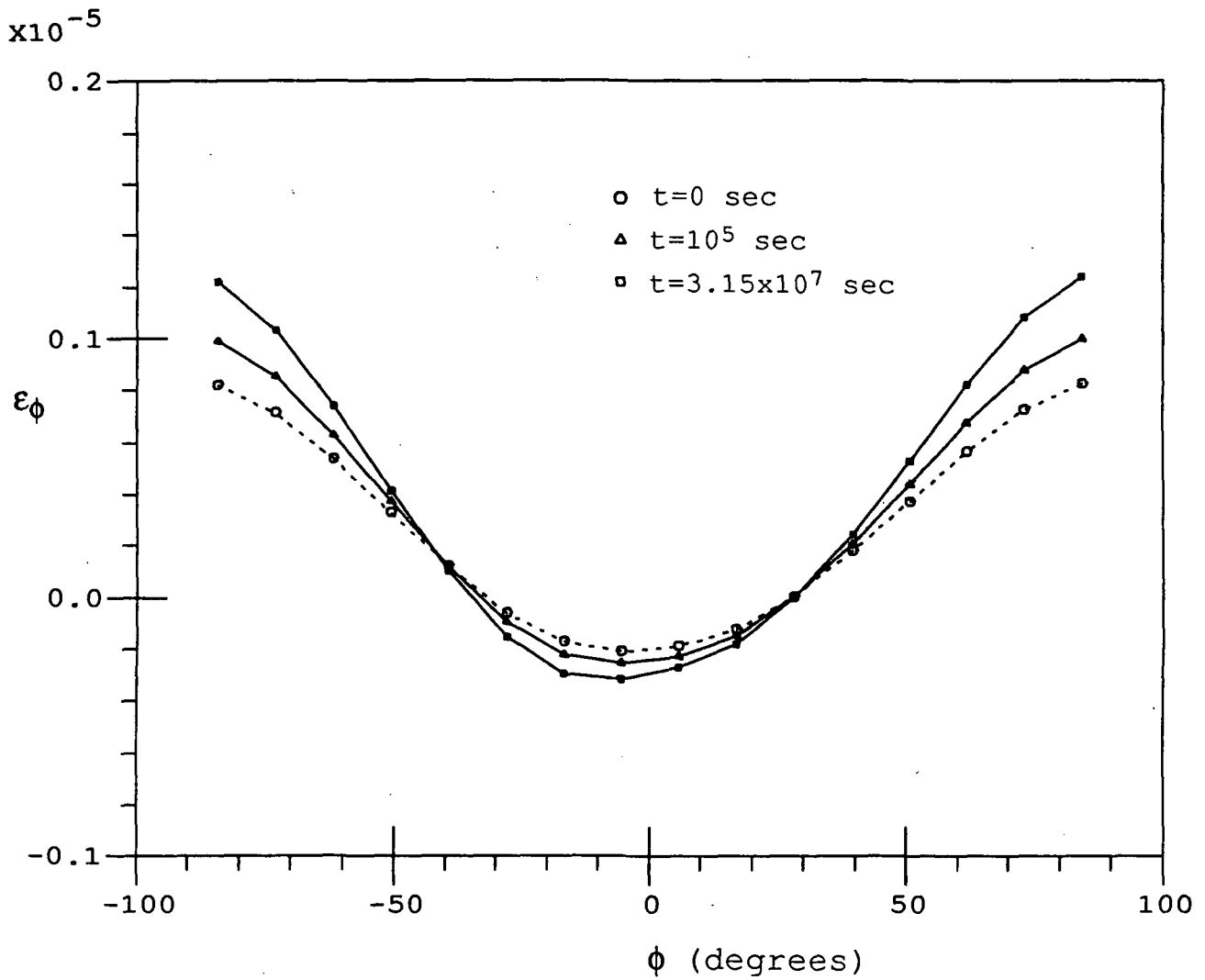Fig. 41 Comparison of elastic ply strains ε_ϕ with the 2-D solution for a $(90/-45/90/45)_S$ laminate

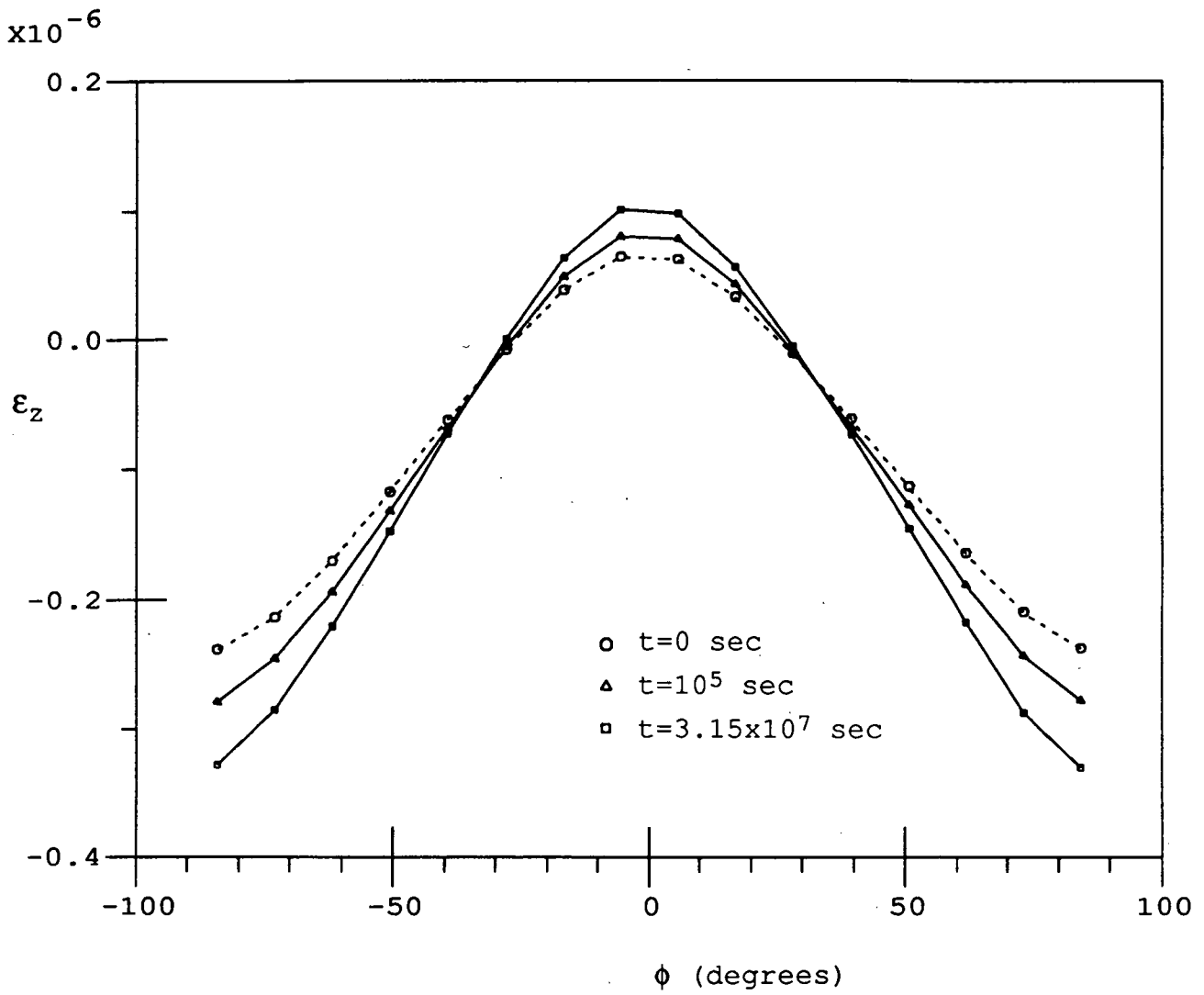Fig. 42 Circumferential strain ε_ϕ in the 90° ply of a (90/-45/90/45)$_s$ laminate

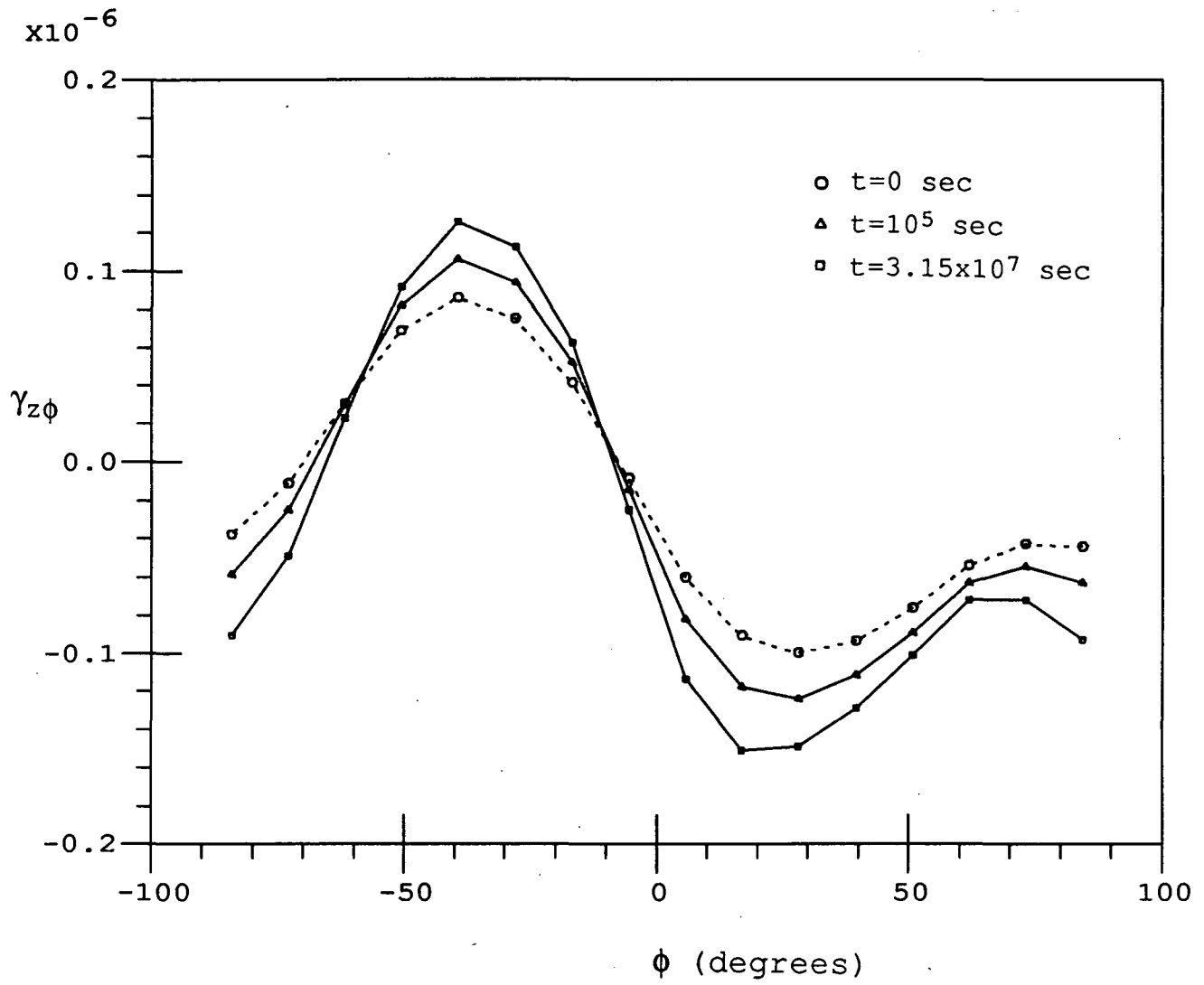Fig. 43 Transverse strain ε_z in the 90° ply of a $(90/-45/90/45)_s$ laminate

Fig. 44 Transverse shear strain $\gamma_{z\phi}$ in the 90° ply of a $(90/-45/90/45)_S$ laminate